of BMP signaling enhances hematovascular development in lateral mesoderm in zebrafish (24). Wnt-induced BMP inhibition is also reported by previous studies showing that Wnt/β-catenin signaling attenuates the expression of BMP4 during neurogenesis (25) and promotes the expression of follistatin in mouse embryonal carcinoma cells (26). However, it should be noted that Wnt-mediated inhibition of BMP signal is context-dependent, because Wnt3a induces the expression of BMP4 in a different cell type (27).

Collectively, our present study indicates that Wnt signals have developmental stage-specific, biphasic, and antagonistic effects on both cardiogenesis and hematopoiesis/vasculogenesis (Fig. 5) and provides important clues to the dissection of cardiogenic signaling pathways during embryogenesis. It also demonstrates that differentiating ES cells represent a useful model system for the dissection of complex regulatory networks that control organogenesis during embryonic development.

Materials and Methods

Reagents. Recombinant mouse Dkk-1, mouse Fz8/Fc, mouse noggin/Fc chimera, mouse Follistatin 288, and human BMP4 proteins were purchased from R&D (Minneapolis, MN). The glycogen synthase kinase-3β inhibitor, BIO, was from Calbiochem (La Jolla, CA). Wnt3a protein was purified as described (28). Elution buffer for Wnt3a protein contains 1% CHAPS and 30 mM imidazole. Same amount of elution buffer was added to the culture medium when using purified Wnt3a protein.

ES Cell Culture and Differentiation Protocol. The 129/Ola-derived ht7 ES cells (29) and hcgp7 ES cells (14) were used in this study. ES cells were maintained on gelatin-coated dishes without feeder cells by using growth medium containing 2,000 units/ml leukemia inhibitory factor (ESGRO; Chemicon, Hampshire, U.K.). For differentiation, 500 ES cells in 30-μl aliquots of (DM; growth medium without leukemia inhibitory factor) were cultured in hanging drop for 3 days. On the third day, the resultant individual EBs were transferred to gelatin-coated 48-well culture plates or a 35-mm dish. To evaluate the differentiation efficiency of ES cells, 48-well plates were monitored every day under a microscope to detect the appearance of spontaneously contracting cardiomyocytes, and the percentage of the EBs that exhibited spontaneous contraction was calculated as differentiation efficiency. More than 200 wells were observed to calculate differentiation efficiency at each time point. The medium was changed every other day. The day when hanging drop culture was started was defined as day 0.

RT-PCR and Quantitative Real-Time PCR. Total RNA extraction and DNase treatment were performed by using the SV total RNA isolation Kit (Promega, Madison, WI). RT-PCR was performed as described (10). Every PCR condition was confirmed to be within the semiquantitative range for specific genes and primer pairs. Expression of β-actin was used as internal control. Real-time PCR was performed by using the LightCycler (Roche, Indianapolis, IN) according to the manufacturer's instructions. Individual PCR products were analyzed by melting-point analysis. β-Actin was used as an internal control to normalize for RNA amounts. Relative levels of gene expression were normalized to the β-actin gene by using the comparative Ct method according to the manufacturer's instructions. Primer sequences for both semiquantitative and quantitative PCR are available upon request.

Western Blotting. Western blotting was performed as described (10). Signal was detected by using ECL detection kit (Amersham Biosciences, Piscataway, NJ).

Immunohistochemistry. Immunohistochemistry was performed as described (30). Mouse monoclonal antisarcomeric myosin heavy chain (MF20; Developmental Studies Hybridoma Bank maintained at the University of Iowa, Department of Biological Sciences, Iowa City, IA) was used as a primary antibody, and FITC-conjugated secondary antibody was applied to visualize expression of specific proteins. Before mounting, nuclei were stained with Topro3 (Molecular Probes, Eugene, OR). Images of samples were taken by laser confocal microscopy (Radiance 2000; Bio-Rad Laboratories, Hercules, CA). For morphometric analysis for the expression of sarcomeric myosin heavy chain stained with MF20, all aspects of cell processing, immunostaining, and imaging were rigorously standardized. To exclude the possibility that variations in immunostaining on different samples affected the morphometric data, all samples in the same data set were immunostained and analyzed at the same time. Digital images were obtained from at least four EBs using the ×10 objective lens. Four images from at least three independent immunostained samples were used for morphometric analysis. The MF20-positive area was calculated as fold increase to that of control EB induced to differentiate into cardiomyocytes with no extra treatment.

FACS Analysis. FACS was performed by using EPICS ALTRA (Beckman Coulter, Fullerton, CA). Cells were dissociated by using 0.05% trypsin (Invitrogen) in PBS and stained with phycoerythrin (PE)-conjugated anti-CD31, -CD34, or -CD45 (all from e-bioscience, San Diego, CA) for 30 min on ice and washed twice with PBS supplemented with 2% FBS. PE and GFP were detected by using a 488-nm argon laser.

Statistical Analysis. Data are expressed as mean ± standard deviation. The significance of differences among means was evaluated by using ANOVA, followed by Fisher's probable least-squares difference test for multiple comparisons. Significant differences were defined as $P < 0.05$.

We thank Hitoshi Niwa (Osaka University, Osaka, Japan) for the ht7 ES cells. This work was supported in part by grants from the Japanese Ministry of Education, Science, Sports, and Culture; the Japan Health Sciences Foundation; Health and Labor Sciences; and the Japan Medical Association (to I.K.); and by a Japan Heart Foundation Young Investigator's Research Grant (to A.T.N.).

1. Logan CY, Nusse R (2004) *Annu Rev Cell Dev Biol* 20:781–810.
2. Reya T, Clevers H (2005) *Nature* 434:843–850.
3. Yamaguchi TP (2001) *Curr Biol* 11:R713–R724.
4. Kimelman D (2006) *Nat Rev Genet* 7:360–372.
5. Marvin MJ, Di Rocco G, Gardiner A, Bush SM, Lassar AB (2001) *Genes Dev* 15:316–327.
6. Schneider VA, Mercola M (2001) *Genes Dev* 15:304–315.
7. Tzahor E, Lassar AB (2001) *Genes Dev* 15:255–260.
8. Wu X, Golden K, Bodmer R (1995) *Dev Biol* 169:619–628.
9. Park M, Wu X, Golden K, Axelrod JD, Bodmer R (1996) *Dev Biol* 177:104–116.
10. Naito AT, Akazawa H, Takano H, Minamino T, Nagai T, Aburatani H, Komuro I (2005) *Circ Res* 97:144–151.
11. Nakamura T, Sano M, Songyang Z, Schneider MD (2003) *Proc Natl Acad Sci USA* 100:5834–5839.
12. Keller G (2005) *Genes Dev* 19:1129–1155.
13. Ema M, Takahashi S, Rossant J (2006) *Blood* 107:111–117.
14. Hidaka K, Lee JK, Kim HS, Ihm CH, Iio A, Ogawa M, Nishikawa S, Kodama I, Morisaki T (2003) *FASEB J* 17:740–742.
15. Frasch M (1995) *Nature* 374:464–467.
16. Schultheiss TM, Burch JB, Lassar AB (1997) *Genes Dev* 11:451–462.
17. Shi Y, Katsev S, Cai C, Evans S (2000) *Dev Biol* 224:226–237.
18. Zhang H, Bradley A (1996) *Development (Cambridge, UK)* 122:2977–2986.
19. Monzen K, Shiojima I, Hiroi Y, Kudoh S, Oka T, Takimoto E, Hayashi D, Hosoda T, Habara-Ohkubo A, Nakaoka T, *et al.* (1999) *Mol Cell Biol* 19:7096–7105.
20. Huber TL, Kouskoff V, Fehling HJ, Palis J, Keller G (2004) *Nature* 432:625–630.
21. Lindsley RC, Gill JG, Kyba M, Murphy TL, Murphy KM (2006) *Development (Cambridge, UK)* 133:3787–3796.
22. Kirstetter P, Anderson K, Porse BT, Jacobsen SE, Nerlov C (2006) *Nat Immunol* 7:1048–1056.
23. Scheller M, Huelsken J, Rosenbauer F, Taketo MM, Birchmeier W, Tenen DG, Leutz A (2006) *Nat Immunol* 7:1037–1047.
24. Gupta S, Zhu H, Zon LI, Evans T (2006) *Development (Cambridge, UK)* 133:2177–2187.
25. Baker JC, Beddington RS, Harland RM (1999) *Genes Dev* 13:3149–3159.
26. Willert J, Epping M, Pollack JR, Brown PO, Nusse R (2002) *BMC Dev Biol* 2:8.
27. Winkler DG, Sutherland MS, Ojala E, Turcott E, Geoghegan JC, Shpektor D, Skonier JE, Yu C, Latham JA (2005) *J Biol Chem* 280:2498–2502.
28. Kishida S, Yamamoto H, Kikuchi A (2004) *Mol Cell Biol* 24:4487–4501.
29. Niwa H, Miyazaki J, Smith AG (2000) *Nat Genet* 24:372–376.
30. Naito AT, Tominaga A, Oyamada M, Oyamada Y, Shiraishi I, Monzen K, Komuro I, Takamatsu T (2003) *Exp Cell Res* 291:56–69.

THE JOURNAL OF BIOLOGICAL CHEMISTRY VOL. 281, NO. 52, pp. 40242–40251, December 29, 2006

Interaction of FoxO1 and TSC2 Induces Insulin Resistance through Activation of the Mammalian Target of Rapamycin/p70 S6K Pathway*

Received for publication, August 23, 2006, and in revised form, October 30, 2006 Published, JBC Papers in Press, October 31, 2006, DOI 10.1074/jbc.M608116200

Yongheng Cao[‡], Yuji Kamioka[§], Norihide Yokoi[¶], Toshiyuki Kobayashi[‖], Okio Hino[‖], Masafumi Onodera[**], Naoki Mochizuki[§], and Jun Nakae[‡1]

From the [‡]Department of Clinical Molecular Medicine, Division of Diabetes, Digestive and Kidney Disease, Kobe University Graduate School of Medicine, Kobe 650-0017, the [§]Department of Structural Analysis, National Cardiovascular Center Research Institute, 5-7-1 Fujishirodai, Suita, Osaka 565-8565, [¶]Division of Cellular and Molecular Medicine, Kobe University Graduate School of Medicine, Kobe 650-0017, the [‖]Department of Experimental Pathology, Cancer Institute, Japanese Foundation for Cancer Research, 1-37-1 Kami-ikebukuro, Toshima-ku, Tokyo 170-8455, and [**]Advanced Biomedical Applications, Graduate School of Comprehensive Human Sciences, University of Tsukuba, Tsukuba 305-8575, Japan

Both TSC2 (tuberin) and forkhead transcription factor FoxO1 are phosphorylated and inhibited by Akt and play important roles in insulin signaling. However, little is known about the relationship between TSC2 and FoxO1. Here we identified TSC2 as a FoxO1-binding protein by using a yeast two-hybrid screening with a murine islet cDNA library. Among FoxOs, only FoxO1 can be associated with TSC2. The physical association between the C terminus of TSC2 (amino acids 1280–1499) and FoxO1 degrades the TSC1-TSC2 complex and inhibits GTPase-activating protein activity of TSC2 toward Rheb. Overexpression of wild type FoxO1 enhances p70 S6K phosphorylation, whereas overexpression of TSC2 can reverse these effects. Knockdown of endogenous FOXO1 in human vascular endothelial cells decreased phosphorylation of p70 S6K. Prolonged overexpression of wild type FoxO1 enhanced phosphorylation of serine 307 of IRS1 and decreased phosphorylation of Akt and FoxO1 itself even in the presence of serum. These data suggest a novel mechanism by which FoxO1 regulates the insulin signaling pathway through negative regulation of TSC2 function.

Forkhead transcription factors of the FoxO (Forkhead box-containing protein, O subfamily) family are conserved across many species. In *Caenorhabditis elegans*, DAF-16, the FoxO orthologue, is downstream of the DAF-2/AGE-1/AKT signaling pathway (1, 2). Loss-of-function of *daf-2*, *age-1*, or *akt* causes life span extension in a *daf-16*-dependent manner (3). In *Drosophila*, the life span is extended over 50% by ablation of insulin-producing cells or mutations of genes encoding the insulin-like receptor (*dInR*) or its receptor substrate (*chico*) (4). Similarly, dInR phosphorylates and inactivates dFOXO, the *Drosophila* homologue of DAF-16/FOXO (5). In mammals, InsR/IGF1R-PI3K-Akt signaling inhibits transcription by FoxO1, FoxO3a, and FoxO4 (6). These proteins possess a forkhead DNA binding domain consisting of around 110 amino acids and a transactivation domain in the C terminus. FoxOs bind to consensus FoxO-binding sites (GTAAA(C/T)A, T(G/A)TTTAC) in the promoter region of their target genes and activate gene expression (7). It has been reported that FoxOs cause cell cycle arrest through induction of *p27*, *p21*, cyclin B, *polo-like kinase*, the retinoblastoma family-related protein p130 and cyclin G2, apoptosis through induction of *Fas* ligand and *Bim*, DNA repair through *GADD45*, stress resistance through MnSOD, and regulation of glucose and lipid metabolism through *G6pase*, *apoC-III*, and *Igfbp-1* (8). Several FoxO-binding proteins, which include co-activators, transcription factors, signaling molecules, and Sirt1, a NAD-dependent deacetylase, have also been identified (8). These FoxO-binding molecules regulate FoxO-dependent transcription and vice versa. However, there have been few reports that described identification of FoxO-binding proteins by comprehensive strategies.

The PI3K[2]-Akt pathway is also important for growth factor stimulation of mammalian target of rapamycin (mTOR) signaling (9). The primary mechanism by which Akt activates mTOR signaling appears to be through direct phosphorylation and inhibition of TSC2 (also known as tuberin). TSC1 (also known as hamartin) and TSC2 were first identified as genes mutated in patients with tuberous sclerosis complex (TSC), an autosomal dominant disease. Affected patients suffer from hamartomas in a wide spectrum of organs. TSC1 and TSC2 physically associate *in vivo* and form a heterodimeric complex (10–12). TSC2 has been directly linked to cell size regulation by the discovery that mutation in dTsc2 leads to the gigas (large cell) phenotype (13).

* This work was supported by the 21st Century COE Program "Center of Excellence for Signal Transduction Disease: Diabetes Mellitus as a Model" grant from the Ministry of Education, Culture, Sports, Science and Technology of Japan. The costs of publication of this article were defrayed in part by the payment of page charges. This article must therefore be hereby marked "*advertisement*" in accordance with 18 U.S.C. Section 1734 solely to indicate this fact.

[1] To whom correspondence should be addressed: Dept. of Clinical Molecular Medicine, Division of Diabetes, Digestive and Kidney Diseases, Kobe University Graduate School of Medicine, 7-5-1 Kusunoki-cho, Chuo-ku, Kobe 650-0017, Japan. Tel.: 81-78-382-5374; Fax: 81-78-382-5379; E-mail: nakaej@med.kobe-u.ac.jp.

[2] The abbreviations used are: PI3K, phosphatidylinositol 3-kinase; mTOR, mammalian target of rapamycin; TSC, tuberous sclerosis complex; DMEM, Dulbecco's modified Eagle's medium; HUVEC, human vascular endothelial cell; siRNA, small interfering RNA; RNAi, RNA interference; ANOVA, analysis of variance; WT, wild type; EGFP, enhanced green fluorescent protein; GST, glutathione *S*-transferase; GAP, GTPase-activating protein; HA, hemagglutinin.

Recent studies revealed that the TSC1-TSC2 complex functions downstream of Akt and upstream of target of rapamycin to restrict cell growth and cell proliferation (14–17). Akt-phosphorylation of TSC2 leads to the functional inactivation of the TSC1-TSC2 complex and results in mTOR activation leading to phosphorylation of two main mTOR substrates, ribosomal p70 S6 kinase (p70 S6K) and eukaryotic initiation factor 4E-binding protein (4E-BP1), and elevated mRNA translation (18–20). The TSC2 C-terminal region has homology with the catalytic domain of GTPase-activating proteins (GAPs). An inhibitory target of TSC1-TSC2 has been identified as Ras homologue enriched in brain (Rheb), a small GTPase. GTP-bound Rheb is bound to and activates mTOR (21, 22).

There have been several reports about molecules, which regulate TSC2 function. Energy depletion inhibits mTOR signaling through AMP-activated kinase phosphorylation of TSC2, although it is not know how AMP-activated kinase phosphorylation of TSC2 enhances the ability of TSC1–TSC2 to inhibit downstream signaling to Rheb (23–25). The hypoxia-inducible gene, regulated in development and damage responses (REDD1), is also induced by energy depletion, and this leads to inhibition of mTOR complex 1 signaling to p70 S6K in a TSC2-dependent manner (26). It is important to identify molecules that regulate TSC2 function because these molecules may affect the activity of mTOR/p70 S6K signaling and finally determine the activity of PI3K/Akt pathway through a negative feedback loop (27).

In this study, we identified TSC2 as a novel FoxO1-binding protein by a yeast two-hybrid screening using a murine islet cDNA library. Binding of FoxO1 to TSC2 in cytoplasm inhibits TSC2 function and results in activation mTOR/p70 S6K and inhibition of Akt activity through negative feedback on IRS protein, leading eventually to feedback activation of FoxO1. Here we demonstrate a novel mechanism by which FoxO1 regulates activity of mTOR/p70 S6K signaling pathway and of FoxO1 itself through association with TSC2.

EXPERIMENTAL PROCEDURES

Antibodies and Plasmids—We purchased anti-FLAG (M2) and anti-tubulin from Sigma; anti-c-Myc (9E10), anti-TSC2 (C-20 and N-19), anti-FOXO1 (H128), anti-FOXO1 (N18), anti-IRS2 from Santa Cruz Biotechnology; anti-HA (12CA5) from Roche Applied Science; anti-p70 S6K, anti-phospho-p70 S6K (Thr(P)-389), anti-phospho-FOXO1 (Ser(P)-256), anti-Akt, anti-phospho-Akt (Thr(P)-308 and Ser(P)-473), and anti-phospho-IRS-1 (Ser(P)-307) from Cell Signaling Technology; anti-TSC1 from Zymed Laboratories Inc.; anti-IRS1 from Upstate Biotechnology, Inc.; and anti-GFP from Dr. Michiyuki Matsuda, Osaka University. We used pCAG/FLAG-rTSC2DEE, pMT2/FLAG-p70 S6K (28), pCMV5/cMyc/FoxO1 (29), pCMV5/cMyc/FoxO3a (30), pTB701-FLAG-FOXO4 (31), pCA-EGFP-Rheb (32), and adenoviral vectors encoding wild type or mutant FoxO1 (30). The pCAG/FLAG-rTSC2DEE was constructed by ligation of N-terminal FLAG-tagged full-length cDNA of rTSC2 with pCAG-GS vector (33, 34).

Construction of Expression Vectors—For mutagenesis of FoxO1, we performed overlap extension PCR using pCMV5/cMyc/ADA FoxO1 as a template as described previously (35). For construction of pCMV5/cMyc/T24A/S253A/S316A (3A), the following mutagenic primers were used: primer 1, 5′-AGA GCT GCG GCC ATG GAC AAC-3′, corresponding to nucleotide 844–864, and primer 2, 5′-GTT GTC CAT GGC CGC AGC TCT-3′, corresponding to nucleotide 864–844.

Yeast Two-hybrid Screen—Amino acids 424–550 of the murine FoxO1 were cloned in-frame into the GAL4 DNA-binding domain plasmid pGBKT7 (Clontech). The GAL4 activation domain cDNA library of murine islets was constructed as described previously (36). AH109 yeast strain was used for the library search. The transformation was performed as described in the Clontech Matchmaker two-hybrid system 3 protocol. The transformants were plated on SD/−Ade/−His/−Leu/−Tyr plates in the presence of galactose and then were incubated at 30 °C for 3–4 days. Positive interaction was identified by strong β-galactosidase activity. Individual positive clones were isolated by YEASTMAKER™ yeast plasmid isolation kit (BD Biosciences) and were sequenced by ABI310 automated DNA sequencer and analyzed for homology with sequences in the GenBank™ data base using the BLAST algorithm.

Cell Culture, Transfection, and Viral Transduction—HEK293 cells were cultured in DMEM containing 10% fetal calf serum. SV40-transformed hepatocytes used in these studies have been described in previous publication (29). Human vascular endothelial cells (HUVEC) were cultured in HuMedia-EB2 (KURABO) supplemented with 2% fetal calf serum, 10 ng/ml human recombinant epidermal growth factor, 1 μg/ml hydrocortisone, 5 ng/ml human recombinant fibroblast growth factor, and 10 μg/ml heparin. Transient transfection was performed using Lipofectamine (Invitrogen) according to manufacturer's protocol. Adenoviral infection was described in a previous publication (30). We transduced SV40-transformed hepatocytes by incubating them with adenoviral preparations at 10–50 multiplicities of infection for 2 h.

Cell Isolation and Culture—Brown adipocytes and their precursor cells were isolated from newborn wild type mice by collagenase digestion as described previously (37). Preadipocytes were immortalized by infection with the retroviral vector pGCDNsamIRES-Puro, encoding SV40T antigen (38) and selected with puromycin (1 μg/ml). Preadipocytes were grown to confluence in culture medium supplemented with 50 nM insulin and 50 nM triiodothyronine (differentiation medium) (day 0). Adipocyte differentiation was induced by treating confluent cells for 24 h in differentiation medium further supplemented with 0.5 mM isobutylmethylxanthine, 0.5 μM dexamethasone, and 0.125 mM indomethacin. After induction, cells were changed back to differentiation medium, which was then changed every day. At day 5, cells were harvested and used for experiments.

Western Blot Analysis—We lysed cells in buffer containing 50 mM Tris-HCl (pH 7.6), 250 mM NaCl, 1% Nonidet P-40, 0.5% deoxycholate, 0.1% SDS, and protease inhibitors (Roche Applied Science). After centrifugation to remove insoluble material, each 30 μg of sample was electrophoresed in SDS-PAGE, and Western blotting was performed. For immunoprecipitation, cell lysates were diluted with buffer containing 50

mM Tris-HCl (pH 7.6), 150 mM NaCl, 0.1% Nonidet P-40, 10% glycerol, 5 mM $MgCl_2$, and protease inhibitors.

In Vitro Translation and Glutathione S-Transferase Fusion Protein Pulldown Assay—The TSC2 deletions were generated by PCR using specific primers, and they were cloned in-frame into the EcoRI and SalI sites of pGEX-4T-1. These fusion proteins were expressed in 20 μl of 50% slurry beads containing ~2 μg of protein (either GST or alone, or fused to deleted TSC2 mutants), resuspended in 350 μl of binding buffer (50 mM Tris-HCl (pH 8.0), 120 mM NaCl, 1 mM EDTA, and 0.5% Nonidet P-40). This was mixed with 10 μl of *in vitro* translated wild type FoxO1 (Promega TnT reticulocyte lysate system kit). Binding was performed for 6 h at 4 °C. The beads were then washed four times with the binding buffer and resuspended in 2× SDS-PAGE sample buffer. Samples were then subjected to SDS-PAGE and transferred to a nitrocellulose membrane; the blot was incubated with anti-FOXO1 antibody and developed with an ECL detection system (Amersham Biosciences).

Immunofluorescence—Immunofluorescence using SV40-transformed hepatocytes was performed as described previously (35). After transient transfection with pCAG/FLAG-TSC2 using Lipofectamine (Invitrogen), SV40-transformed hepatocytes were transduced with adenovirus encoding HA-tagged wild type or ADA-FoxO1. HA-tagged FoxO1 was visualized with anti-HA monoclonal antibody and fluorescein isothiocyanate-conjugated anti-mouse IgG, and TSC2 was visualized with anti-TSC2 polyclonal antibody and rhodamine-conjugated anti-rabbit IgG.

Measurement of GTP- and GDP-bound Rheb—SV40-transformed hepatocytes were cultured in 6-well plates and co-transfected with pCAG/FLAG-rTSC2DEE and pCA-EGFP-Rheb using Lipofectamine 2000 reagent (Invitrogen) and subsequently transduced with an adenovirus encoding WT FoxO1. At 48 h after transfection, the cells were washed once with phosphate-free DMEM (DMEM without sodium phosphate and sodium pyruvate; Invitrogen) and incubated with 1 ml of phosphate-free DMEM for 90 min. Cells were then incubated with 25 μCi of [^{32}P]phosphate/ml (GE healthcare) for 4 h. After the labeling, cells were lysed with prechilled lysis buffer (0.5% Triton X-100, 20 mM Tris (pH 7.5), 150 mM NaCl, 20 mM $MgCl_2$, 1 mM phenylmethylsulfonyl fluoride, 10 μg of leupeptin/ml, 10 μg of aprotinin/ml; 600 μl per well of a 6-well plate). To avoid lysing the nuclei, the cells were incubated with lysis buffer for just 30 s with gentle shaking. The lysates were then centrifuged at 12,000 × *g* for 15 min at 4 °C. The supernatant (500 μl) was transferred to a fresh tube. Sixteen microliters of NaCl (500 mM) was added to 160 μl of supernatant to inhibit GAP activity in the lysates. To immunoprecipitate pCA-EGFP-Rheb, anti-green fluorescent protein and protein A-agarose (GE Healthcare) were added to the supernatant and incubated for 3 h at 4 °C. The beads were washed with lysis buffer two times and with wash buffer (20 mM Tris (pH 7.5), 150 mM NaCl, 20 mM $MgCl_2$) one time at 4 °C. The Rheb-bound nucleotides were eluted with 15 μl of elution buffer (20 mM Tris (pH 7.5), 20 mM EDTA, 2% SDS) at 68 °C for 10 min. Ten microliters of eluted nucleotides was then applied onto polyethyleneimine-cellulose plates. Before applying sample, the plate was soaked in methanol and dried with a hair dryer. The bottom portion of the plate was immersed in methanol again, and the plate was placed in a sealed chromatography chamber that was filled with 0.75 M KH_2PO_4 (pH 3.4) to a depth of 1 cm. The chamber was closed, and the solvent was allowed to ascend to the top of the plate. The plate was then removed and air-dried. GTP and GDP resolved by thin layer chromatography were visualized and quantified by a BAS-5000 (Fuji Film).

Design and Transfection of siRNAs—We used BLOCK iT RNAi Designer (Invitrogen) to identify target siRNAs and used Stealth RNAi (Invitrogen). The FOXO1-specific sequence was 5′-AACUGCAGAUGUCUGCUGAGCAUGU-3′. HUVECs were transfected with Stealth RNAi using Lipofectamine 2000 according to the manufacturer's instruction (Invitrogen). At 48 h after transfection, cells were harvested and used for Western blotting.

Statistics—We calculated descriptive statistics and ANOVA followed by Fisher's test using the Statview software (SAS Institute Inc.).

RESULTS

Identification of TSC2 as a FoxO1-binding Protein—To identify proteins that bind to FoxO1, we performed a yeast two-hybrid screen using GAL4-FoxO1 fragment (amino acids 424–550) as bait and a murine islet cDNA library as prey. About 2 × 10^6 transformants were tested. The strongest colony was isolated and was found to encode the C-terminal fragment of murine TSC2 (amino acids 1280–1815). To confirm the interaction between TSC2 and FoxO1, we co-transfected HEK293 cells with pCAG/FLAG-rTSC2DEE and pCMV5/cMyc-WT FoxO1, and we immunoprecipitated cell lysates using normal mouse IgG or anti-c-Myc mouse antibody and blotted with anti-FLAG antibody. Reciprocal immunoprecipitation/immunoblotting using anti-FLAG and anti-c-Myc antibodies showed that the exogenously expressed FoxO1 could interact with FLAG-tagged full-length-TSC2 (Fig. 1*a*).

Furthermore, to investigate whether endogenous FoxO1 is physically associated with TSC2 or not, cell lysates from brown adipocytes immortalized by SV40-T antigen were immunoprecipitated with anti-FOXO1 (Fig. 1*b*, *lane 2*) or anti-TSC2 (Fig. 1*b*, *lane 5*) and followed by an immunoblotting with using antibodies against TSC2 (Fig. 1*b*, *lanes 1–3, top panel*) or FOXO1 (Fig. 1*b*, *lanes 4–6, top panel*). In this cell line, both FoxO1 and TSC2 are expressed abundantly. Our results showed that endogenous FoxO1 was associated with endogenous TSC2 (Fig. 1*b*). These results suggest that FoxO1 interacts physically with TSC2 *in vivo*.

TSC2 Binds to Only FoxO1 among FoxO Family Members—FoxOs consist of FoxO1, FoxO3a, and FoxO4. These molecules have highly conserved motifs, which include forkhead DNA binding domain, three Akt phosphorylation sites, and several acetylation sites. Therefore, it is interesting to investigate whether TSC2 is associated with other FoxOs or not. To examine whether all three FoxOs can interact with TSC2 equally, we transfected SV40-transformed hepatocytes with cMyc-FoxO1, -FoxO3a, or FLAG-FOXO4 and immunoprecipitated lysates with antibody against TSC2 or normal rabbit serum and immunoblotted with antibody against c-Myc or FLAG. This co-immunoprecipitation study demonstrated that only FoxO1 could

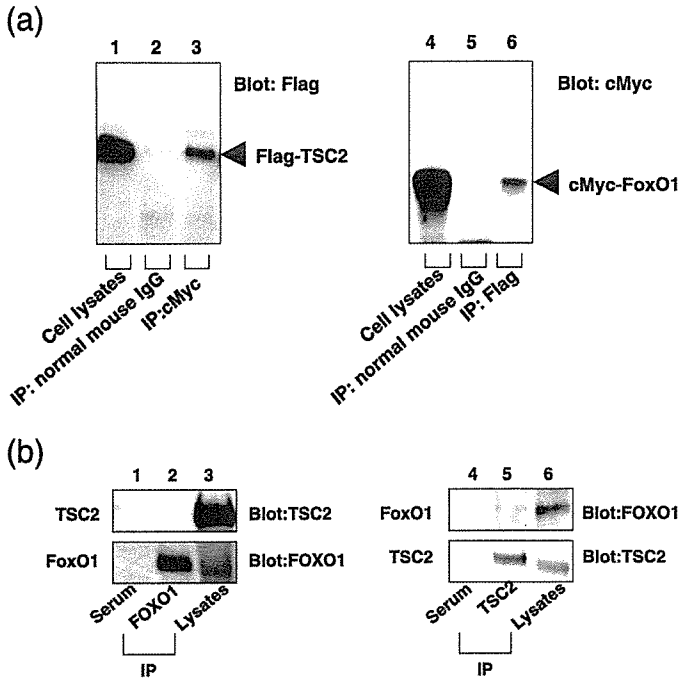

FIGURE 1. **Interaction of FoxO1 and TSC2.** *a*, EK293 cells were co-transfected with c-Myc-WT FoxO1 and FLAG-TSC2 transiently. c-Myc FoxO1 was immunoprecipitated (*IP*) with anti-c-Myc mouse monoclonal antibody (*lane 3*) or normal mouse IgG (*lane 2*), and the immune complexes were assessed for the presence of FLAG-TSC2 by Western blotting (*Blot*) with anti-FLAG antibody. Reciprocal experiment was done by immunoprecipitation with anti-FLAG (*lane 6*) or normal mouse IgG (*lane 5*) and Western blotting with anti-c-Myc antibody. *b*, cell lysates from immortalized brown adipocytes were immunoprecipitated with normal rabbit serum (*lanes 1* and *4*), anti-FOXO1 (*lane 2*), or anti-TSC2 rabbit polyclonal antibody (*lane 5*) and immunoblotted with anti-TSC2 (the *upper panel* from *lanes 1–3*) or anti-FOXO1 goat polyclonal antibody (N18) (the *upper panel* from *lanes 4–6*).

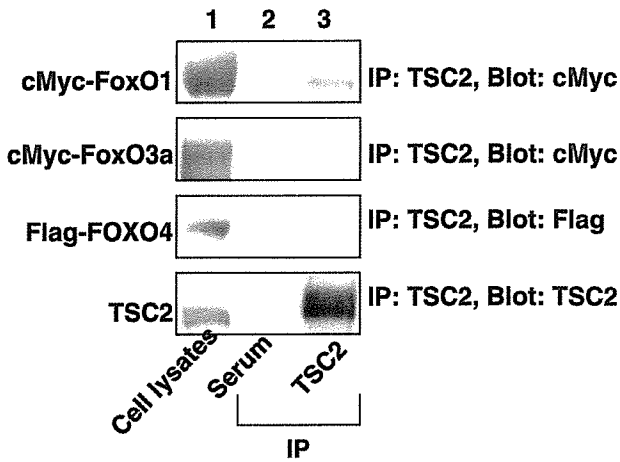

FIGURE 2. **Only FoxO1 binds to TSC2 among FoxO family members.** Cell lysates from SV40-transformed hepatocytes transfected with c-Myc-FoxO1 (*top panel*), -FoxO3a (*2nd panel*), or FLAG-FOXO4 (*3rd panel*) were immunoprecipitated (*IP*) with normal rabbit serum (*lane 2*) or anti-TSC2 rabbit polyclonal antibody (*lane 3*) and immunoblotted with anti-c-Myc mouse (*top* and *2nd panels*) or anti-FLAG mouse monoclonal antibody (*3rd panel*).

interact with endogenous TSC2 (Fig. 2, *lane 3, top panel*). These data suggest that FoxO1 interacts with TSC2 among FoxOs specifically.

Identification of FoxO1-binding Site in TSC2 Protein—To examine whether FoxO1 interacts with TSC2 directly, we constructed several glutathione *S*-transferase (GST) fusion TSC2

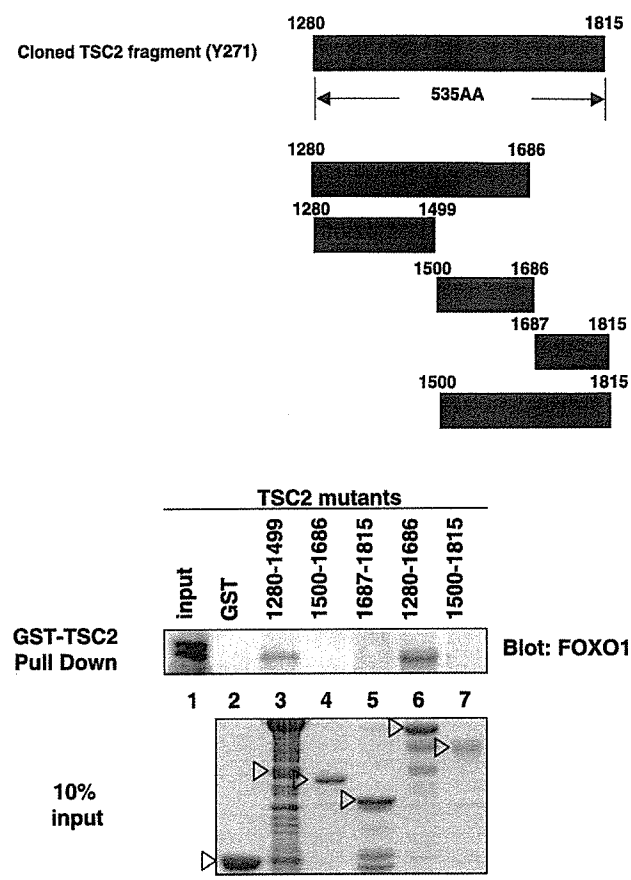

FIGURE 3. **Identification of the FoxO1-binding site in TSC2.** *a*, schematics of TSC2 deletion mutants are shown. The top deleted mutant fragment of TSC2 is cloned by a yeast two-hybrid assay. *b*, GST-TSC2 deleted mutants, indicated by *arrowheads*, were subjected to pulldown assay. Aliquots of *in vitro* translated wild type FoxO1 was incubated with glutathione-Sepharose beads coated with bacterially expressed GST alone or GST-TSC2 for 6 h at 4 °C. The retained *in vitro* translated FoxO1 proteins were separated on SDS-PAGE followed by Western blotting with anti-FOXO1 antibody. The *bottom panel* shows 10% of input of GST-mutant TSC2s stained with Coomassie Blue.

fragments. Because the yeast two-hybrid screening identified the C-terminal fragment of TSC2 (amino acids 1280–1815), we constructed several deleted Tsc2 mutants in this region (Fig. 3*a*). Using *in vitro* translated wild type FoxO1, pulldown assays with GST-deleted TSC2 fusion proteins were performed and showed that FoxO1 interacted with the C-terminal TSC2 fragment (amino acids 1280–1686) directly. The FoxO1-binding site on TSC2 protein encompasses amino acids 1280–1499 (Fig. 3*b*, *lane 3*), located near the GAP domain of TSC2. These data suggest that FoxO1 binds to TSC2 directly.

FoxO1 Co-localizes with TSC2 in Cytoplasm—To examine subcellular localization of the FoxO1/TSC2 interaction, we transfected SV40-transformed hepatocytes with pCAG/FLAG-rTSC2DEE, transduced them with adenovirus encoding with HA-WT or ADA FoxO1 (30), and performed immunofluorescence using anti-TSC2 polyclonal and anti-HA monoclonal antibodies. In this cell line, even in the absence of serum, 70–80% of wild type FoxO1 was located in cytoplasm until 48 h after transduction (data not shown), where it co-localized with TSC2. In contrast, FLAG-TSC2 failed to co-localize with constitutively nuclear HA-tagged ADA FoxO1 (Fig. 4*a*). These data demonstrate that FoxO1 co-localizes with TSC2 in cytoplasm.

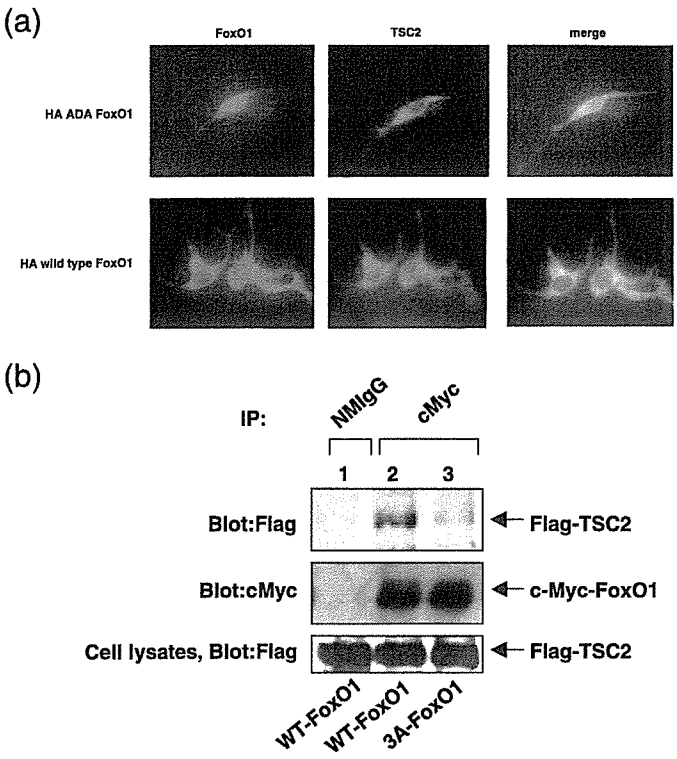

FIGURE 4. **Co-localization and co-immunoprecipitation of FoxO1 with TSC2 in cytoplasm.** *a*, FoxO1 is co-localized with TSC2 in cytoplasm and not in nucleus. SV40-transformed hepatocytes were transiently transfected with FLAG-TSC2 followed by transduction with adenovirus encoding a constitutively active HA-ADA FoxO1 (*upper panel*) or HA wild type FoxO1 (*lower panel*), and immunofluorescence was performed as described under "Experimental Procedures." *b*, constitutively active mutant FoxO1 (3A) in which three Akt phosphorylation sites (Thr-24, Ser-253, and Ser-316) were substituted to alanine residues binds to TSC2 weakly compare with wild type FoxO1. SV40-transformed hepatocytes were co-transfected with c-Myc-WT FoxO1 (*lanes 1* and *2*) or -3A FoxO1 (*lane 3*) and FLAG-TSC2 transiently. Cell lysates were immunoprecipitated (*IP*) with anti-c-Myc mouse monoclonal antibody (*lanes 2* and *3*) or normal mouse IgG (*lane 1*) and Western-blotted with anti-FLAG (*upper panel*), anti-c-Myc (*middle panel*). The *lower panel* shows Western blotting with anti-FLAG using cell lysates.

Furthermore, to examine whether FoxO1 interacts with TSC2 in cytoplasm, we used a constitutively active mutant FoxO1 (3A FoxO1) in which all three Akt phosphorylation sites were mutated to alanine (T24A/S253A/S316A; 3A FoxO1) and performed co-immunoprecipitation experiments in the same cell line. Although exogenous WT FoxO1 interacted with TSC2 as well as in HEK293 cells (Fig. 1*a*), the 3A FoxO1 interacted with TSC2 weakly compared with wild type FoxO1 (Fig. 4*b*, *lanes 2* and *3*). These data suggest the possibility that FoxO1 may associate with TSC2 in cytoplasm.

FoxO1 Inhibits TSC2 and Enhances p70 S6K Phosphorylation—TSC2 regulates cellular function mainly by their inhibitory effects on mTOR and its targets p70 S6K and 4E-BP1. It is important to elucidate whether binding of FoxO1 to TSC2 affects the activity of the mTOR/p70 S6K pathway. To investigate the effects of the FoxO1/TSC2 interaction on the mTOR pathway, we transfected SV40-transformed hepatocytes with FLAG-p70 S6K followed by transduction with adenovirus encoding HA-WT FoxO1 or -ADA FoxO1, which is localized in the nucleus and active constitutively and is immunoprecipitated with anti-FLAG monoclonal antibody and blotted with anti-phospho-p70 S6K (Thr(P)-389) antibody. After serum deprivation for 24 h, p70 S6K is dephosphorylated, and insulin increases phosphorylation of p70 S6K (Fig. 5*a*, *lanes 1* and *2* and *lanes 6* and *7*). However, even in the absence of insulin, p70 S6K was phosphorylated in a dose-dependent manner of transduced WT FoxO1 (Fig. 5, *a*, *lanes 3–5*, and *b*, *left panel*). As described above, in this cell line, even after serum deprivation for 24 h, around 70 – 80% of transduced wild type FoxO1 is located in the cytoplasm (data not shown) and is phosphorylated (Fig. 5*a*, *lanes 3–5*). These data indicate that FoxO1 is constantly phosphorylated in this cell line even in the absence of serum and insulin. In contrast, p70 S6K was dephosphorylated in cells transduced with the ADA-FoxO1 (Fig. 5, *a*, *lanes 8–10*, and *b*, *right panel*). These data suggest that FoxO1 in cytosol enhances p70 S6K phosphorylation.

To confirm whether enhanced phosphorylation of p70 S6K by FoxO1 is mediated through binding to TSC2, we overexpressed FLAG-TSC2 in SV40-transformed hepatocytes transduced with adenovirus encoding HA-WT FoxO1, and we investigated the effects on phosphorylation of p70 S6K. Overexpression of TSC2 decreased phosphorylation of p70 S6K (Fig. 5*c*, *lanes 1* and *2*). Overexpression of WT FoxO1 enhanced phosphorylation of p70 S6K (Fig. 5*c*, *lanes 1* and *3*). Even in the presence of WT FoxO1, overexpression of TSC2 decreased phosphorylation of p70 S6K (Fig. 5*c*, *lanes 3* and *4*). These data suggest that cytoplasmic FoxO1 enhances phosphorylation of p70 S6K through association with endogenous TSC2. These data also suggest the possibility that cytoplasmic FoxO1 may affect an inhibitory action of TSC2 onto mTOR and activate mTOR.

FoxO1 Functions Upstream of mTOR for Activation of p70 S6K—To investigate whether enhanced phosphorylation of p70 S6K by overexpression of WT FoxO1 is mediated through mTOR activation, we treated cells with rapamycin (25 nM) and examined effects on p70 S6K phosphorylation. Overexpression of WT FoxO1 enhanced phosphorylation of p70 S6K (Fig. 6, *lanes 2* and *3*). In contrast, treatment with rapamycin abolished p70 S6K phosphorylation induced by overexpression of FoxO1 (Fig. 6, *lane 4*). These data suggest that FoxO1 enhances phosphorylation of p70 S6K through activation of mTOR and mTOR functions downstream of FoxO1 for p70 S6K phosphorylation.

FoxO1 Reduces the Association between TSC1 and TSC2—Dimerization of TSC2 with TSC1 is important for functional inhibition on the mTOR/p70 S6K pathway. To elucidate the mechanism of how FoxO1 inhibits TSC2, we transduced HUVEC with adenovirus encoding WT FoxO1 and immunoprecipitated cell lysates with anti-TSC2 (Fig. 7*a*, *lanes 3–5*), anti-TSC1 (Fig. 7*a*, *lanes 8–10*), or anti-HA antibody (Fig. 7*a*, *lanes 13–15*) and immunoblotted with anti-TSC1, anti-TSC2, or anti-HA antibody. Overexpression of WT FoxO1 increased association with TSC2 (Fig. 7*a*, *lanes 3–5*, *bottom panel*). Co-immunoprecipitation of TSC2 and TSC1 was decreased in a dose-dependent manner of transduced FoxO1 (Fig. 7*a*, *lanes 3–5* and *lanes 8–10*, *top panel*). TSC1 does not show any physical association with transduced FoxO1 (Fig. 7*a*, *lanes 8–10*, *bottom panel*, and *lanes 13–15*, *bottom panel*). Furthermore, immunoblotting with anti-TSC2 antibody (C-20), which recognizes the C terminus of TSC2, detected a short fragment of

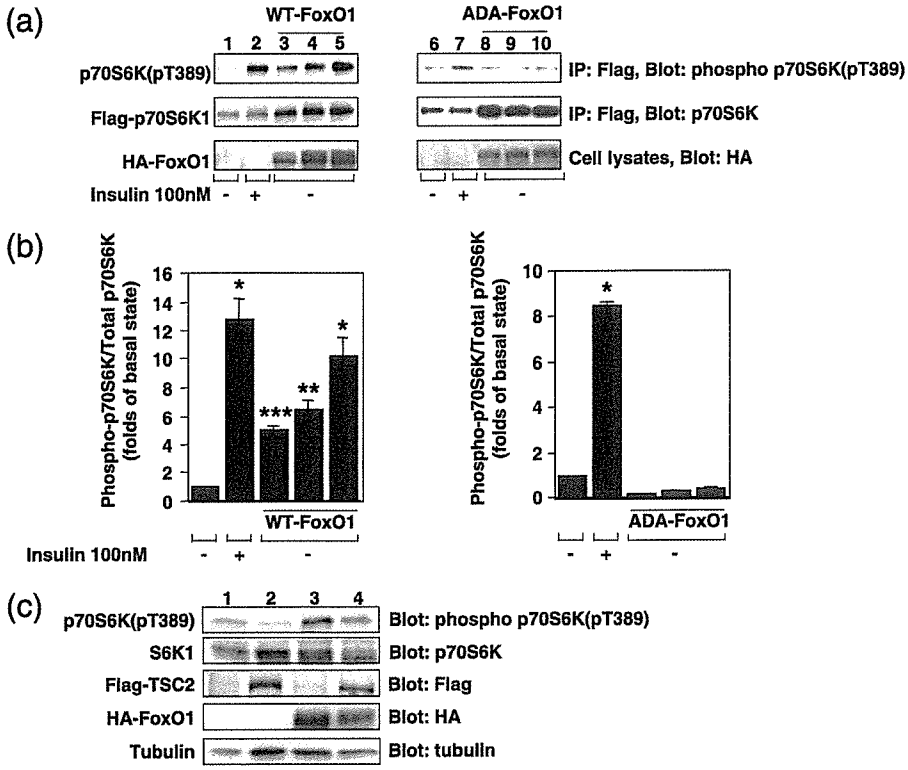

FIGURE 5. **TSC2 inhibits enhanced phosphorylation of p70 S6K induced by overexpression of WT FoxO1.** *a*, SV40-transformed hepatocytes were transfected with FLAG-p70 S6K transiently followed by transduction with adenovirus encoding HA-WT (*lanes 3–5*) or HA-ADA FoxO1 (*lanes 8–10*). At 24 h after transfection, serum deprivation was performed for 16 h, and cells were stimulated with (*lanes 2* and *7*) or without insulin (100 nM) for 30 min. Cell lysates were immunoprecipitated (*IP*) with anti-FLAG monoclonal antibody and blotted with anti-phospho-p70 S6K (pT389) (*upper panel*) or anti-p70 S6K antibody (*middle panel*). The *lower panel* shows Western blotting of transduced FoxO1 using anti-HA monoclonal antibody. *b*, ratio of phospho-p70 S6K to total p70 S6K was calculated by measuring density of bands blotted with anti-phospho-p70 S6K or total p70 S6K using NIH Image 1.62. Data were shown as folds of basal level of phospho-p70 S6K in nontransduced cells in the absence of insulin and represent mean ± S.E. from three independent experiments. *Asterisks* indicate statistically significant differences compared with the basal state (*, $p < 0.005$; **, $p < 0.02$; ***, $p < 0.05$ by one-factor ANOVA). *c*, SV40-transformed hepatocytes were transfected transiently with (*lanes 2* and *4*) or without pCAG/FLAG-TSC2 (*lanes 1* and *3*) and followed by transduction with adenovirus encoding WT FoxO1 (*lanes 3* and *4*). Cells were harvested and lysed at 48 h after transduction. Cell lysates were immunoblotted with the indicated antibodies.

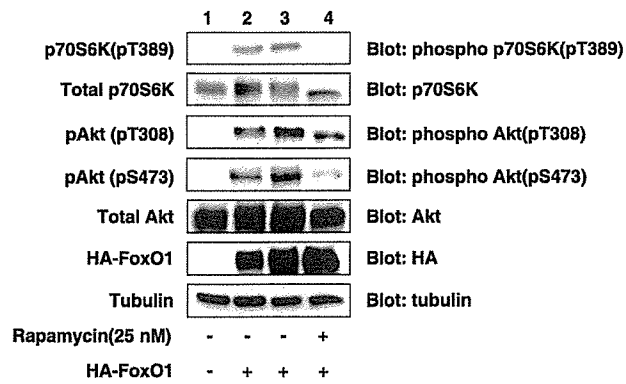

FIGURE 6. **FoxO1 enhances p70 S6K phosphorylation in a rapamycin-sensitive manner.** SV40-transformed hepatocytes were transduced with HA-WT FoxO1. At 24 h after transduction, cells were stimulated with (*lane 4*) or without (*lanes 1–3*) rapamycin (25 nM) for 24 h and harvested. Cell lysates were immunoblotted with the indicated antibodies.

TSC2, which was immunoprecipitated with FoxO1 (Fig. 7*a*, *lanes 14–15, top panel*). This short fragment of TSC2 was also detected in SV40-transformed hepatocytes (data not shown). In another set of experiments in HUVEC, WT FoxO1 decreased total amounts of full-length TSC2, which was detected by both C-20 (Fig. 7*b*, *top panel*) and N-19, which recognized the N terminus of TSC2 (Fig. 7*b*, *2nd panels*). Furthermore, the amount of short band of TSC2 was increased in a dose-dependent manner of transduced WT FoxO1 (Fig. 7*b*, *top panel*). However, we could not detect the fragmented N terminus of TSC2 by immunoblotting with N-19 antibody. These data indicate that WT FoxO1 interacts with TSC2 through its C-terminal domain, fragmented TSC2, and disrupts heterodimeric complex between TSC1 and TSC2.

Physical Association of FoxO1 with TSC2 Inhibits GAP Activity toward Rheb—From this study, FoxO1 binds to amino acids 1280–1499 of TSC2, which is near the GAP domain of TSC2. Therefore, it is possible to speculate that binding of FoxO1 may inhibit the GAP activity of TSC2. To investigate whether FoxO1 inhibits the GAP activity of TSC2 toward Rheb, we transfected cells with pCAG/FLAG-rTSC2DEE and pCA-EGFP-Rheb transiently followed by transduction with adenovirus encoding WT FoxO1 in SV40-transformed hepatocytes, and we examined guanyl nucleotide binding by EGFP-Rheb. Overexpression of TSC2 decreased %GTP by 33% compared with non-transfected cells (Fig. 8, *a*, *lanes 1* and *2*, and *b*). In contrast, overexpression of both TSC2 and FoxO1 increased %GTP by 30% compared with TSC2-transfected cells (Fig. 8*a*, *lanes 2* and *3*, and *b*). These data suggest that FoxO1 inhibits the GAP activity of TSC2 toward Rheb.

Knockdown of FOXO1 Reduces Phosphorylation of p70 S6K in HUVEC—If endogenous FoxO1 binds to TSC2 and inhibits its function, decreased expression of FoxO1 activates TSC2 and inhibits mTOR-p70 S6K pathway. To investigate whether endogenous FoxO1 inhibits TSC2, we transfected HUVEC with siRNA of FOXO1. In this cell line, both endogenous FOXO1 and TSC2 are expressed abundantly (Fig. 9 and data not shown). Knockdown of FOXO1 in HUVEC decreased FOXO1 protein level by 90% (Fig. 9, *a*, *top panel*, and *b*). Knockdown of FOXO1 inhibited phosphorylation of p70 S6K (Fig. 9, *2nd panel*). These data suggest that endogenous FOXO1 inhibits TSC2 and regulates phosphorylation of p70 S6K *in vivo*.

Prolonged Overexpression of FoxO1 Enhances Phosphorylation of Ser-307 of IRS-1—It has been reported that p70 S6K might be implicated in a negative feedback loop to suppress insulin signaling (27). From this study, we demonstrated that

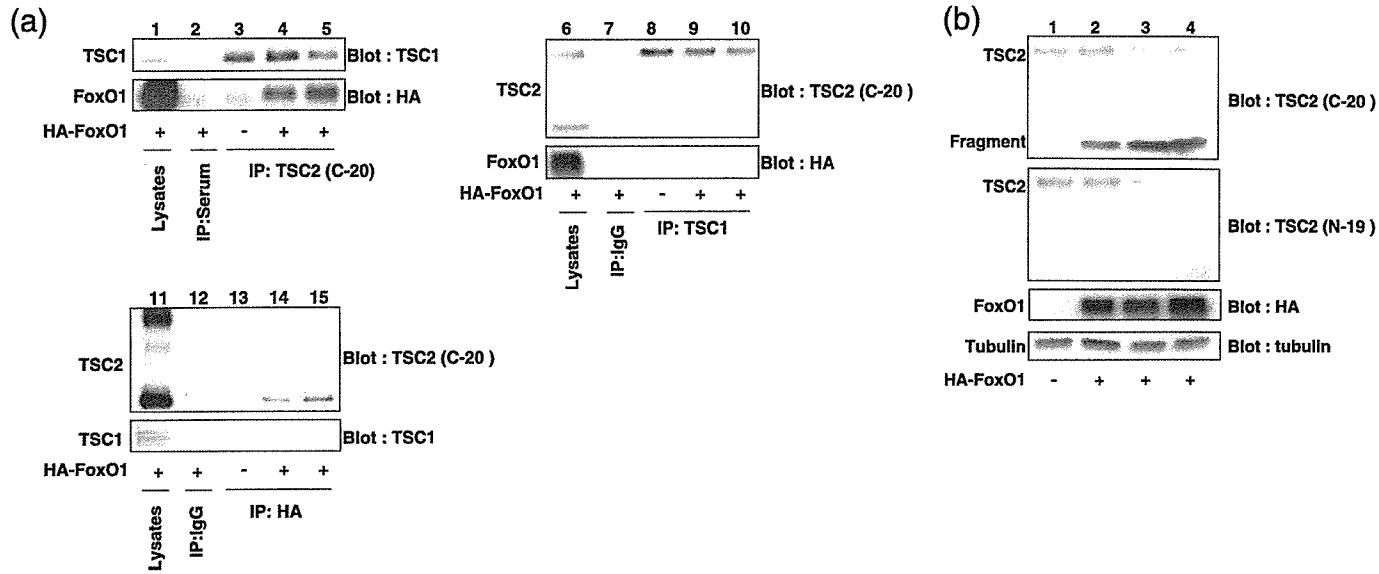

FIGURE 7. **FoxO1 reduces the association between TSC1 and TSC2.** *a*, HUVEC were transduced with adenovirus encoding HA-WT FoxO1 and were harvested 48 h later. Cell lysates were immunoprecipitated (*IP*) with normal rabbit serum (*lane 2*), normal mouse IgG (*lanes 7* and *12*), anti-TSC2 (*lanes 3–5*), anti-TSC1 (*lanes 8–10*), or anti-HA (*lanes 13–15*) and immunoblotted with the indicated antibodies. *Lanes 1, 6,* and *11* indicate cell lysates immunoblotted with the indicated antibodies. *b*, HUVEC were transduced with adenovirus encoding HA-WT FoxO1 (*lanes 2–4*) in a dose-dependent manner. At 48 h after transduction, cells were harvested and lysed. Lysates were immunoblotted with the indicated antibodies.

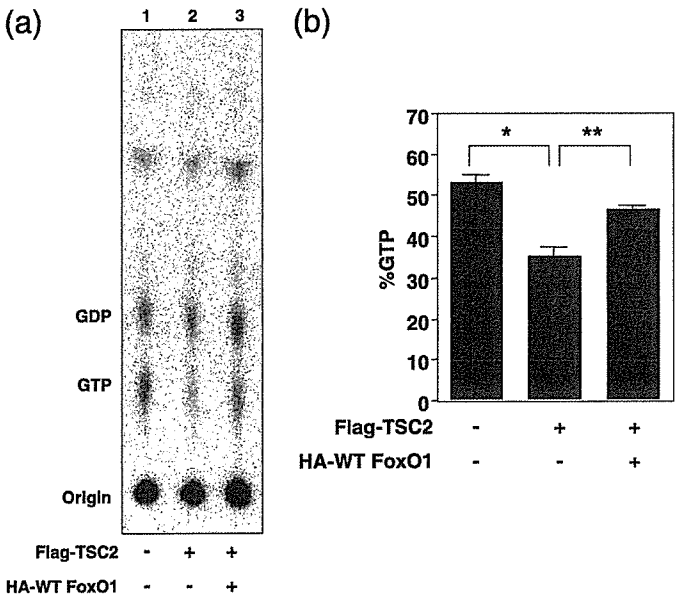

FIGURE 8. **FoxO1 inhibits GAP activity of TSC2 toward Rheb.** *a*, EGFP-Rheb in SV40-transformed hepatocytes labeled with [^{32}P]orthophosphate was immunoprecipitated with anti-GFP antibody, and the ratio of GTP to GDP bound Rheb was determined by PhosphorImager analysis following one-dimensional thin layer chromatography. Representative experiment was shown. *b*, the values of %GTP were data from three independent experiments and were shown as mean ± S.E. A *single asterisk* indicates a statistically significant difference between nontransfected and cells transfected with pCAG/FLAG-rTSC2DEE ($p < 0.001$ by one-factor ANOVA). A *double asterisk* indicates a statistically significant difference between cells transfected with pCAG/FLAG-rTSC2DEE and with both pCAG/FLAG-rTSC2DEE and WT FoxO1 ($p < 0.005$ by one-factor ANOVA).

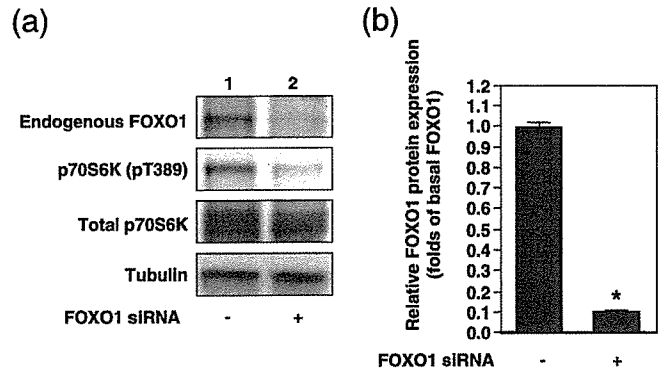

FIGURE 9. **Knockdown of endogenous FOXO1 reduces phosphorylation of p70 S6K in HUVEC.** *a*, HUVEC were transfected as described under "Experimental Procedures." At 48 h after transfection, cells were harvested and lysed. Cell lysates were immunoblotted with the indicated antibodies. *b*, efficiency of knockdown was calculated by measuring density of bands blotted with anti-FOXO1 using NIH Image 1.62. Data were shown as folds of FOXO1 protein expression in nontransfected cells and represent mean ± S.E. from three independent experiments. A *single asterisk* indicates a statistically significant difference ($p < 0.001$ by one-factor ANOVA).

cytosolic FoxO1 bound to and inhibited TSC2 and enhanced phosphorylation of p70 S6K. We speculate that enhanced phosphorylation of p70 S6K may lead to phosphorylation of serine 307 in IRS-1, which is one of the phosphorylation sites by p70 S6K (39), and finally to decreased phosphorylation of Akt and FoxO1 itself. To investigate whether FoxO1-TSC2 binding affects phosphorylation of serine 307 of IRS1 or not, we transduced SV40-transformed hepatocytes with adenoviruses encoding LacZ or WT FoxO1 and cultured cells in the presence of serum, and we examined phosphorylation of serine 307 of IRS-1 in a time course study. Phosphorylation of p70 S6K in WT FoxO1-transduced cells at 48 and 72 h is increased compared with LacZ-transduced cells because of inhibition of TSC2 by overexpression of FoxO1 from the previous experiments (Fig. 10*a*, *3rd top panel*). Amounts of total IRS1 protein level showed no significant differences between LacZ- and WT FoxO1-transduced cells (Fig. 10*a*, *lanes 1–6, 2nd top panel*). However, phosphorylation of serine 307 of IRS1 in WT FoxO1-transduced cells is increased significantly compared with LacZ-transduced cells at 72 h after transduction (Fig. 10, *a*, *lanes 3* and *6, top panel,* and *b*). Furthermore, at 72 h after transduction, phosphorylation of both threonine 308 and serine 473 of

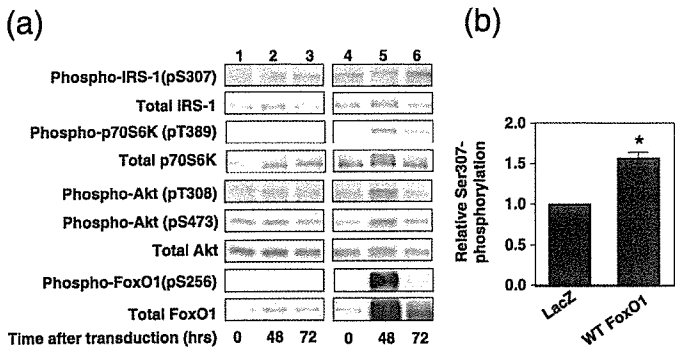

FIGURE 10. **Prolonged overexpression of wild type FoxO1 enhances phosphorylation of serine 307 of IRS1.** *a*, SV40-transformed hepatocytes were transduced with adenovirus encoding LacZ (*lanes 2* and *3*) or HA wild type FoxO1 (*lanes 5* and *6*) and cultured with complete medium at the indicated time. Culture medium was exchanged every day. Cell lysates were electrophoresed in SDS-PAGE and blotted with the indicated antibodies. *b*, intensity of bands blotted with anti-phospho-IRS1 (*pS307*) at 72 h after transduction were measured using NIH Image 1.62. Data represent mean ± S.E. from three independent experiments. An *asterisk* indicates a statistically significant difference ($p < 0.005$ by one-factor ANOVA).

Akt was decreased even in the presence of serum and also phosphorylation of FoxO1 itself was decreased. These data suggest that FoxO1-TSC2 binding leads to enhanced phosphorylation of serine 307 of IRS-1 protein through increased phosphorylation of p70 S6K and finally inhibits phosphorylation of Akt and FoxO1 itself even in the presence of serum.

DISCUSSION

In this study, we identified TSC2 as a novel FoxO1-binding protein by a yeast two-hybrid screening using a murine islet cDNA library. FoxOs interact with several kinds of protein and regulate their function and vice versa. For example, FoxO1 binds to the transcriptional co-activator PGC-1α, and PGC-1α potentiates FoxO1-dependent transcription of gluconeogenic genes (40). Acetylation by Cbp/P300 and deacetylation by Sirt1 regulates transcriptional activity of FoxOs (6). Therefore, it is important for understanding the mechanism of how FoxO1 is regulated to identify FoxO1-binding proteins. However, there are few reports about the identification of FoxO1-binding proteins using comprehensive strategies.

We used a murine islet cDNA library for identification of FoxO1-binding proteins because FoxO1 is expressed in pancreatic β-cells abundantly and has been reported already to play an important role for compensatory hypertrophy of β-cells under insulin resistance (41–43). Therefore, we speculated that it might be easy to identify FoxO1-binding proteins by using an islet cDNA library.

One of interesting findings in this study is that only FoxO1 binds to TSC2 among FoxOs. We used a fragment (amino acids 424–550) of the C terminus of FoxO1 as bait for a yeast two-hybrid screening. Amino acid sequences in this region of FoxO1, except the LXXLL motif (amino acids 459–463) (44), have low similarity among FoxOs. Therefore, it is reasonable for only FoxO1 to associate with TSC2 physically. These findings suggest the hypothesis that FoxO1 may have specific roles *in vivo*. Studies using genetically modified mice, such as knockout and transgenic mice, support this hypothesis. FoxO1-null mice die at embryonic day 10.5 from defects in angiogenesis (45). Heterozygous mutant mice of FoxO1 are viable and rescue phenotype in heterozygous knock-out mice of insulin receptor or high fat diet-induced mice (46, 47). FoxO3a-null mice are viable, and their main defect is an age-dependent female infertility because of premature activation of ovarian follicles (45, 48). FoxO4-null mice are also viable and do not show any overt phenotype (45). Each FoxO family member may have a different function *in vivo* because of distinct patterns or different regulations of each protein.

Several studies in *Drosophila* demonstrated that TSC2 forms complex with TSC1, and this complex is important for cell growth regulation (13, 49–51). This complex is assembled with rapid kinetics post-translationally serving to stabilize TSC1 and TSC2, which are ubiquitylated and degraded in their monomeric forms (18, 52, 53). TSC2 interacts with TSC1 through the N-terminal region and appears to function as a heterodimer (49, 50, 51). We demonstrated that FoxO1 bound to the C-terminal domain (amino acids 1280–1499) of TSC2, and thereafter TSC2 was fragmented when FoxO1 was overexpressed in HUVEC as shown in Fig. 7*a*. This C-terminal fragment of TSC2 was still bound to FoxO1. However, TSC1 could not bind to this C-terminal fragment of TSC2 any more because TSC1 bound to the N terminus of TSC2. After these events, the association between TSC1 and TSC2 was reduced to negatively regulate its function. The C terminus of TSC2 has a GAP domain (amino acids 1517–1674) (54). It has been demonstrated that TSC2 functions as a GAP toward Rheb, which is a small G protein implicated genetically as a positive regulator of mTOR (55–58), and that TSC2 represses Rheb function (59–62). This study demonstrated that FoxO1 binds to an adjacent region near the GAP domain of TSC2 directly and inhibits the GAP activity toward Rheb. Inhibition of TSC2 by FoxO1 leads to enhanced phosphorylation of p70 S6K. In contrast, we demonstrated that knockdown of endogenous FOXO1 by around 90% decreased phosphorylation of p70 S6K in HUVEC. These data indicate that endogenous FOXO1 has an important role for regulation of phosphorylation of p70 S6K and might suggest a novel cross-talk between Akt/FoxO1 and mTOR/p70 S6K pathway through TSC2.

It has been reported that p70 S6K may be implicated in a negative feedback loop to suppress insulin signaling. High fat-dieted *p70 S6K1*$^{-/-}$ mice remained insulin-sensitive, and knockdown of p70 S6K1 also potentiates insulin-induced Akt phosphorylation (39). p70 S6K has an inhibitory effect on Akt activation downstream of insulin receptor. p70 S6K enhances IRS-1 serine phosphorylation, which leads to decreased Akt phosphorylation and causes insulin resistance (39). It has been suggested that p70 S6K mediates IRS-1 serine phosphorylation, disrupting its interaction with IR and leading to its degradation (63). Furthermore, degradation of phosphorylated IRS-1 is mediated by its association with a 14-3-3 family member, which relocates IRS-1 from low density microsomes to the cytosol, where it can be accessed and degraded by the 26 S proteasome (64). In this study, overexpression of WT FoxO1 in SV40-transformed hepatocytes enhanced phosphorylation of serine 307 of IRS-1 and decreased Akt phosphorylation at 72 h after transduction. In concordance with this result, phosphorylation of p70 S6K was enhanced. Finally, phosphorylation of WT FoxO1

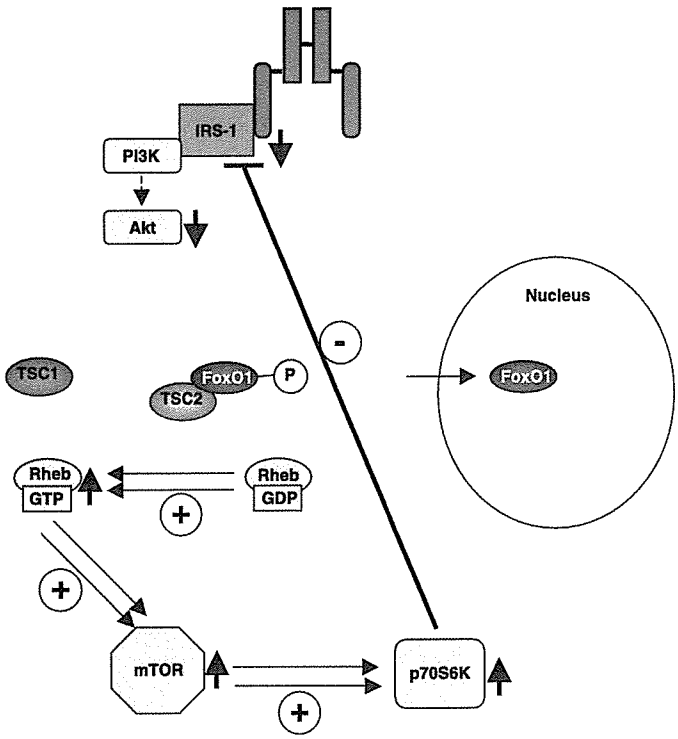

FIGURE 11. **Model depicting effects of interaction between FoxO1 and TSC2 on mTOR/p70 S6K/IRS-1 pathway.** FoxO1 in cytosol binds to TSC2 and dissociates the TSC1-TSC2 complex and inhibits the GAP activity toward Rheb. These events lead to activation of Rheb/mTOR/p70 S6K. Finally, IRS-1/PI3K/Akt pathway is inhibited through a negative feedback. After inactivation of IRS-1/PI3K/Akt pathway, FoxO1 is dephosphorylated and entered into nucleus and activates its target gene expression. A *plus* indicates an active effect, and a *minus* indicates an inhibitory effect.

itself was blunted even in the presence of serum. These data suggest a novel mechanism in which FoxO1 in cytosol can regulate Akt/FoxO1 through the TSC2/mTOR/p70 S6K/IRS1 pathway (Fig. 11).

In conclusion, these studies identified TSC2 as a novel interacting protein with FoxO1 and suggested that FoxO1 could negatively regulate TSC2 function. They suggest a novel cross-talk between Akt/FoxO1 and the mTOR/p70 S6K pathway and propose the possibility that FoxO1 can induce insulin resistance not only through increased gene expression in the nucleus but also through down-regulation insulin signaling in the cytosol. Therefore, regulation of the association between FoxO1 and TSC2 should be a target of therapy of type 2 diabetes.

Acknowledgments—We thank Susumu Seino (Division of Cellular and Molecular Medicine, Kobe University Graduate School of Medicine) for supplying the murine islet cDNA library and kindly making available the laboratory to accomplish this work. We also thank Kenta Hara (Department of Geriatric Medicine, Kobe University Graduate School of Medicine) and Kazuyoshi Yonezawa (Biosignal Research Center, Kobe University) for supplying the pMT2/FLAG-p70 S6K vector.

REFERENCES

1. Ogg, S., Paradis, S., Gottlieb, S., Patterson, G. I., Lee, L., Tissenbaum, H. A., and Ruvkun, G. (1997) *Nature* **389,** 994–999
2. Lin, K., Dorman, J. B., Rodan, A., and Kenyon, C. (1997) *Science* **278,** 1319–1322
3. Lin, K., Hsin, H., Libina, N., and Kenyon, C. (2001) *Nat. Genet.* **28,** 139–145
4. Stocker, H., and Hafen, E. (2000) *Curr. Opin. Genet. Dev.* **10,** 529–535
5. Puig, O., Marr, M. T., Ruhf, M. L., and Tjian, R. (2003) *Genes Dev.* **17,** 2006–2020
6. Accili, D., and Arden, K. C. (2004) *Cell* **117,** 421–426
7. Furuyama, T., Nakazawa, T., Nakano, I., and Mori, N. (2000) *Biochem. J.* **349,** 629–634
8. Greer, E. L., and Brunet, A. (2005) *Oncogene* **24,** 7410–7425
9. Fingar, D. C., and Blenis, J. (2004) *Oncogene* **23,** 3151–3171
10. The European Chromosome 16 Tuberous Sclerosis Consortium (1993) *Cell* **75,** 1305–1315
11. Hay, N., and Sonenberg, N. (2004) *Genes Dev.* **18,** 1926–1945
12. Sparagana, S. P., and Roach, E. S. (2000) *Curr. Opin. Neurol.* **13,** 115–119
13. Ito, N., and Rubin, G. M. (1999) *Cell* **96,** 529–539
14. Gao, X., Zhang, Y., Arrazola, P., Hino, O., Kobayashi, T., Yeung, R. S., Ru, B., and Pan, D. (2002) *Nat. Cell Biol.* **4,** 699–704
15. Goncharova, E. A., Goncharov, D. A., Eszterhas, A., Hunter, D. S., Glassberg, M. K., Yeung, R. S., Walker, C. L., Noonan, D., Kwiatkowski, D. J., Chou, M. M., Panettieri, R. A., Jr., and Krymskaya, V. P. (2002) *J. Biol. Chem.* **277,** 30958–30967
16. Kwiatkowski, D. J., Zhang, H., Bandura, J. L., Heiberger, K. M., Glogauer, M., el-Hashemite, N., and Onda, H. (2002) *Hum. Mol. Genet.* **11,** 525–534
17. Tee, A. R., Fingar, D. C., Manning, B. D., Kwiatkowski, D. J., Cantley, L. C., and Blenis, J. (2002) *Proc. Natl. Acad. Sci. U. S. A.* **99,** 13571–13576
18. Inoki, K., Li, Y., Zhu, T., Wu, J., and Guan, K. L. (2002) *Nat. Cell Biol.* **4,** 648–657
19. Manning, B. D., Tee, A. R., Logsdon, M. N., Blenis, J., and Cantley, L. C. (2002) *Mol. Cell* **10,** 151–162
20. Potter, C. J., Pedraza, L. G., and Xu, T. (2002) *Nat. Cell Biol.* **4,** 658–665
21. Manning, B. D., and Cantley, L. C. (2003) *Trends Biochem. Sci.* **28,** 573–576
22. Li, Y., Corradetti, M. N., Inoki, K., and Guan, K. L. (2004) *Trends Biochem. Sci.* **29,** 32–38
23. Corradetti, M. N., Inoki, K., Bardeesy, N., DePinho, R. A., and Guan, K. L. (2004) *Genes Dev.* **18,** 1533–1538
24. Inoki, K., Zhu, T., and Guan, K. L. (2003) *Cell* **115,** 577–590
25. Shaw, R. J., Bardeesy, N., Manning, B. D., Lopez, L., Kosmatka, M., DePinho, R. A., and Cantley, L. C. (2004) *Cancer Cell* **6,** 91–99
26. Sofer, A., Lei, K., Johannessen, C. M., and Ellisen, L. W. (2005) *Mol. Cell. Biol.* **25,** 5834–5845
27. Um, S. H., D'Alessio, D., and Thomas, G. (2006) *Cell Metab.* **3,** 393–402
28. Hara, K., Yonezawa, K., Kozlowski, M. T., Sugimoto, T., Andrabi, K., Weng, Q. P., Kasuga, M., Nishimoto, I., and Avruch, J. (1997) *J. Biol. Chem.* **272,** 26457–26463
29. Nakae, J., Park, B. C., and Accili, D. (1999) *J. Biol. Chem.* **274,** 15982–15985
30. Nakae, J., Kitamura, T., Silver, D. L., and Accili, D. (2001) *J. Clin. Investig.* **108,** 1359–1367
31. Takaishi, H., Konishi, H., Matsuzaki, H., Ono, Y., Shirai, Y., Saito, N., Kitamura, T., Ogawa, W., Kasuga, M., Kikkawa, U., and Nishizuka, Y. (1999) *Proc. Natl. Acad. Sci. U. S. A.* **96,** 11836–11841
32. Kamioka, Y., Fukuhara, S., Sawa, H., Nagashima, K., Masuda, M., Matsuda, M., and Mochizuki, N. (2004) *J. Biol. Chem.* **279,** 40091–40099
33. Tsuchiya, H., Orimoto, K., Kobayashi, K., and Hino, O. (1996) *Cancer Res.* **56,** 429–433
34. Niwa, H., Yamamura, K., and Miyazaki, J. (1991) *Gene (Amst.)* **108,** 193–199
35. Nakae, J., Barr, V., and Accili, D. (2000) *EMBO J.* **19,** 989–996
36. Nishimura, M., Yokoi, N., Miki, T., Horikawa, Y., Yoshioka, H., Takeda, J., Ohara, O., and Seino, S. (2004) *DNA Res.* **11,** 315–323
37. Klein, J., Fasshauer, M., Ito, M., Lowell, B. B., Benito, M., and Kahn, C. R. (1999) *J. Biol. Chem.* **274,** 34795–34802
38. Nabekura, T., Otsu, M., Nagasawa, T., Nakauchi, H., and Onodera, M. (2006) *Mol. Ther.* **13,** 301–309
39. Um, S. H., Frigerio, F., Watanabe, M., Picard, F., Joaquin, M., Sticker, M., Fumagalli, S., Allegrini, P. R., Kozma, S. C., Auwerx, J., and Thomas, G. (2004) *Nature* **431,** 200–205

40. Puigserver, P., Rhee, J., Donovan, J., Walkey, C. J., Yoon, J. C., Oriente, F., Kitamura, Y., Altomonte, J., Dong, H., Accili, D., and Spiegelman, B. M. (2003) *Nature* **423,** 550–555
41. Kitamura, T., Nakae, J., Kitamura, Y., Kido, Y., Biggs, W. H., III, Wright, C. V., White, M. F., Arden, K. C., and Accili, D. (2002) *J. Clin. Investig.* **110,** 1839–1847
42. Kitamura, Y. I., Kitamura, T., Kruse, J. P., Raum, J. C., Stein, R., Gu, W., and Accili, D. (2005) *Cell Metab.* **2,** 153–163
43. Okamoto, H., Hribal, M. L., Lin, H. V., Bennett, W. R., Ward, A., and Accili, D. (2006) *J. Clin. Investig.* **116,** 775–782
44. Nakae, J., Cao, Y., Daitoku, H., Fukamizu, A., Ogawa, W., Yano, Y., and Hayashi, Y. (2006) *J. Clin. Investig.* **116,** 2473–2483
45. Hosaka, T., Biggs, W. H., III, Tieu, D., Boyer, A. D., Varki, N. M., Cavenee, W. K., and Arden, K. C. (2004) *Proc. Natl. Acad. Sci. U. S. A.* **101,** 2975–2980
46. Nakae, J., Biggs, W. H., Kitamura, T., Cavenee, W. K., Wright, C. V., Arden, K. C., and Accili, D. (2002) *Nat. Genet.* **32,** 245–253
47. Nakae, J., Kitamura, T., Kitamura, Y., Biggs, W. H., III, Arden, K. C., and Accili, D. (2003) *Dev. Cell* **4,** 119–129
48. Castrillon, D. H., Miao, L., Kollipara, R., Horner, J. W., and DePinho, R. A. (2003) *Science* **301,** 215–218
49. Potter, C. J., Huang, H., and Xu, T. (2001) *Cell* **105,** 357–368
50. Gao, X., and Pan, D. (2001) *Genes Dev.* **15,** 1383–1392
51. Tapon, N., Ito, N., Dickson, B. J., Treisman, J. E., and Hariharan, I. K. (2001) *Cell* **105,** 345–355
52. Nellist, M., van Slegtenhorst, M. A., Goedbloed, M., van den Ouweland, A. M., Halley, D. J., and van der Sluijs, P. (1999) *J. Biol. Chem.* **274,** 35647–35652
53. Benvenuto, G., Li, S., Brown, S. J., Braverman, R., Vass, W. C., Cheadle, J. P., Halley, D. J., Sampson, J. R., Wienecke, R., and DeClue, J. E. (2000) *Oncogene* **19,** 6306–6316
54. Li, Y., Inoki, K., and Guan, K. L. (2004) *Mol. Cell. Biol.* **24,** 7965–7975
55. Wienecke, R., Konig, A., and DeClue, J. E. (1995) *J. Biol. Chem.* **270,** 16409–16414
56. Xiao, G. H., Shoarinejad, F., Jin, F., Golemis, E. A., and Yeung, R. S. (1997) *J. Biol. Chem.* **272,** 6097–6100
57. Garami, A., Zwartkruis, F. J., Nobukuni, T., Joaquin, M., Roccio, M., Stocker, H., Kozma, S. C., Hafen, E., Bos, J. L., and Thomas, G. (2003) *Mol. Cell* **11,** 1457–1466
58. Tee, A. R., Manning, B. D., Roux, P. P., Cantley, L. C., and Blenis, J. (2003) *Curr. Biol.* **13,** 1259–1268
59. Inoki, K., Li, Y., Xu, T., and Guan, K. L. (2003) *Genes Dev.* **17,** 1829–1834
60. Zhang, Y., Gao, X., Saucedo, L. J., Ru, B., Edgar, B. A., and Pan, D. (2003) *Nat. Cell Biol.* **5,** 578–581
61. Stocker, H., Radimerski, T., Schindelholz, B., Wittwer, F., Belawat, P., Daram, P., Breuer, S., Thomas, G., and Hafen, E. (2003) *Nat. Cell Biol.* **5,** 559–565
62. Saucedo, L. J., Gao, X., Chiarelli, D. A., Li, L., Pan, D., and Edgar, B. A. (2003) *Nat. Cell Biol.* **5,** 566–571
63. Harrington, L. S., Findlay, G. M., Gray, A., Tolkacheva, T., Wigfield, S., Rebholz, H., Barnett, J., Leslie, N. R., Cheng, S., Shepherd, P. R., Gout, I., Downes, C. P., and Lamb, R. F. (2004) *J. Cell Biol.* **166,** 213–223
64. Craparo, A., Freund, R., and Gustafson, T. A. (1997) *J. Biol. Chem.* **272,** 11663–11669

The EMBO Journal (2006) 25, 2889–2897 | © 2006 European Molecular Biology Organization | All Rights Reserved 0261-4189/06
www.embojournal.org

THE EMBO JOURNAL

Endophilin BAR domain drives membrane curvature by two newly identified structure-based mechanisms

Michitaka Masuda[1,4], Soichi Takeda[2,3,4], Manami Sone[1], Takashi Ohki[1], Hidezo Mori[2], Yuji Kamioka[1] and Naoki Mochizuki[1,*]

[1]Department of Structural Analysis, National Cardiovascular Center Research Institute, Suita, Osaka, Japan, [2]Department of Cardiac Physiology, National Cardiovascular Center Research Institute, Suita, Osaka, Japan and [3]Laboratory of structural biochemistry, RIKEN Harima Institute at SPring-8, Mikazuki-cho, Sayo, Hyogo, Japan

The crescent-shaped BAR (Bin/Amphiphysin/Rvs-homology) domain dimer is a versatile protein module that senses and generates positive membrane curvature. The BAR domain dimer of human endophilin-A1, solved at 3.1 Å, has a unique structure consisting of a pair of helix–loop appendages sprouting out from the crescent. The appendage's short helices form a hydrophobic ridge, which runs across the concave surface at its center. Examining liposome binding and tubulation *in vitro* using purified BAR domain and its mutants indicated that the ridge penetrates into the membrane bilayer and enhances liposome tubulation. BAR domain-expressing cells exhibited marked plasma membrane tubulation *in vivo*. Furthermore, a swinging-arm mutant lost liposome tubulation activity yet retaining liposome binding. These data suggested that the rigid crescent dimer shape is crucial for the tubulation. We here propose that the BAR domain drives membrane curvature by coordinate action of the crescent's scaffold mechanism and the ridge's membrane insertion in addition to membrane binding via amino-terminal amphipathic helix.

The EMBO Journal (2006) **25**, 2889–2897. doi:10.1038/sj.emboj.7601176; Published online 8 June 2006
Subject Categories: membranes & transport; structural biology
Keywords: BAR domain; endophilin; liposome; membrane curvature; membrane insertion

Introduction

Membrane dynamics in a cell, such as membrane budding, tubulation, fission and fusion, is associated with changes in membrane curvature. The crystal structure of amphiphysin BAR (Bin/Amphiphysin/Rvs-homology) domain revealed an unexpected structural identity with arfaptin2, a binding protein to Arf and Rac small GTPases (Tarricone *et al*, 2001), and provided a common structural base for the sensing and the formation of positive curvature membrane by BAR-family proteins (Peter *et al*, 2004).

Endophilins are cytoplasmic proteins containing an N-terminal BAR domain and a C-terminal SH3 domain, and are involved in membrane dynamics (Schuske *et al*, 2003; Galli and Haucke, 2004; Wenk and De Camilli, 2004). There are five endophilin genes in the mammalian genomes, endophilin A1–3 and B1–2. Both A and B types are highly conserved from nematode to human. The most extensively studied one is endophilin-A1, a brain specific protein involved in clathrin-mediated synaptic vesicle endocytosis (Ringstad *et al*, 1997, 2001). Via SH3 domain, endophilins bind to the GTPase dynamin, a membrane scissor, and the polyphosphoinositide phosphatase synaptojanin, a clathrin-uncoater (Ringstad *et al*, 1997; de Heuvel *et al*, 1997; Verstreken *et al*, 2003). The BAR domain of endophilins is classified into the N-BAR subgroup characterized by a short amphipathic helical sequence preceding the consensus BAR-domain sequence (Peter *et al*, 2004). The N-BAR domain of endophilin-A1 binds to liposomes and induces the tubulation *in vitro*, requiring the short amphipathic helical sequence (Farsad *et al*, 2001).

The crescent-shaped BAR dimer structure implies a simple model to drive membrane curvature: the dimer may impress its positively charged concave surface on the negatively charged membrane to form a high-curvature membrane domain (Gallop and McMahon, 2005; McMahon and Gallop, 2005). This curvature-impressing or scaffold mechanism for membrane deformation is based on an assumption that the dimer behaves as a rigid body on the membrane (Zimmerberg and Kozlov, 2006). Although the essential requirement of positively charged residues on the concave surface has been suggested (McMahon and Mills, 2004; Peter *et al*, 2004), there have been no experimental supports for the scaffold mechanism. Here, we show the requirement of the molecular rigidity of the BAR dimer for membrane curvature on the basis of structure-oriented mutational analysis.

By determining the structure of endophilin-A1 BAR domain, we found a distinction from those of the known BAR domains: a helix–loop appendage of 30 amino acids stretch is inserted into the helix I of the canonical BAR domain. A pair of the helices of the appendages forms a hydrophobic ridge, which runs across the center of the concave surface of the dimer. We analyzed the function of this ridge as well as the previously proposed structure, the N-terminal amphipathic helix and the crescent main body, for membrane deformation (Peter *et al*, 2004). N-terminal amphipathic helix is essential for membrane binding. The crescent main body of the BAR dimer is required for impressing its intrinsic curvature to the membrane. The ridge contributes to deform the membrane

*Corresponding author. Department of Structural Analysis, National Cardiovascular Center Research Institute, 5-7-1 Fujishiro-dai, Suita, Osaka 565-8565, Japan. Tel.: +81 6 6833 5012; Fax: +81 6 6835 5461; E-mail: nmochizu@ri.ncvc.go.jp
[4]These authors contributed equally to this work

Received: 15 November 2005; accepted: 8 May 2006; published online: 8 June 2006

presumably by penetrating into the membrane. Our results illustrate how these three components coordinate to induce membrane deformation.

Results

Endophilin-A1 BAR domain has a unique appendage

The structure of the BAR domain of human endophilin-A1 (amino acid 1–247, hereafter EndA1-BAR) was solved at 3.1 Å resolution by a multi-wavelength anomalous dispersion method. The structure of EndA1-BAR dimer is similar to that of amphiphysin (Peter *et al*, 2004) and arfaptin2 (Tarricone *et al*, 2001): a crescent-shaped dimer composed of a 6-helix bundle core and two 3-helix bundle arms extended from the core (Figure 1A). The whole structure of EndA1-BAR dimer can be precisely superimposed on that of amphiphysin and arfaptin (Figure 1B). All three structures show nearly identical dimer shapes. Notably, the present EndA1-BAR structure from a tetragonal crystal packing is almost completely the same as an independent crystal structure from an orthogonal crystal packing (Supplementary Figure 1; and Weissenhorn, 2005). The RMS deviations are 0.63, 0.86 and 0.80 Å for Cα atoms in monomers A, B and dimer, respectively. The structural identity indicates that the crescent shape is stably present in solution. Consistent with previous results (Habermann, 2004; Peter *et al*, 2004), structure-based sequence alignment reveals that these three proteins are poorly conserved in amino-acid sequence including the residues possibly important for the crescent-shape formation (Supplementary Figure 2).

We find a unique structure of the EndA1-BAR, an appendage-like structure protruded from the center of the dimer (Figure 1A). The sequence alignments of the BAR-family proteins indicated that this appendage appears unique to the endophilin-family proteins including nadrin (Habermann, 2004; Peter *et al*, 2004) and the candidates from yeasts (Supplementary Figure 2). The appendage (Q59–Q88) has an N-terminal short helix and a loop of which electron density is mostly missing (N72–G85). The pair of helices appears to stay on the main body and forms a ridge across the center of the concave dimer surface. The helix displays, on its top surface, a series of hydrophobic residues (P62, A63, A66 and M70) aligned 60° against the longitudinal axis of the dimer (Figure 1C). Other than the conserved hydrophobic amino acids of the ridge, the appendage sequences show clear distinction between endophilin-A and endophilin-B (Supplementary Figure 2). The B type endophilins show cytoplasmic localization, presumably being involved in intracellular membrane dynamics (Farsad *et al*, 2001; Modregger *et al*, 2003; Karbowski *et al*, 2004). Analyses of chimeric mutations in the appendage between EndA1-BAR and EndB1-BAR suggest that BAR domain may contribute to defining where to target, plasma membrane or intracellular organ membrane (Supplementary Figure 3).

The appendage's penetration enhances liposome tubulation

To investigate the functional significance of the hydrophobic ridge of the endophilin-specific appendage, we first examined the effects of point mutations in this region (red residues in Figure 1C) on the liposome binding and tubulation activities *in vitro* (Figures 2A and 3). Introduction of membrane-repulsive negative charge (A66D) lost the ability to form tubes from liposomes. Hydrophilic mutations (A63S/A66S (SS) and A63S/A66S/M70Q (SSQ)) reduced the number of tubes (<1/100) and induced three-time enlargement of the tube diameter. In contrast, a bulky hydrophobic residue

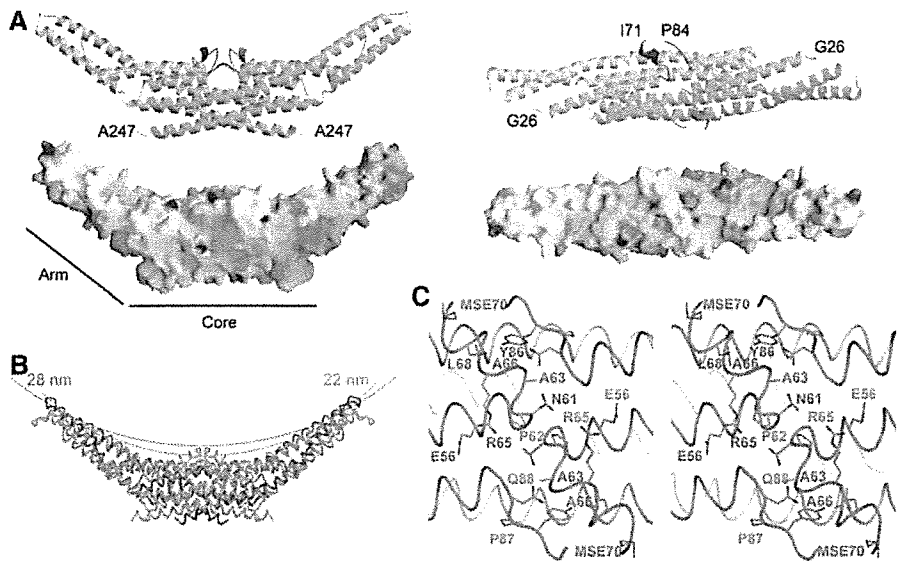

Figure 1 Structure of human endophilin-A1 BAR domain dimer. (**A**) Ribbon representation (a green monomer with a red appendage and a pale-blue monomer with a blue appendage) and surface electrostatic potential (red, $-15\,kTe^{-1}$; blue, $15\,kTe^{-1}$) of the dimer viewed from the side (left) and from the top (right). The numbered amino-acid residues are the first and the last ones in consecutive polypeptide segments determined in this model. (**B**) Comparison of three BAR domain structures in trace representation. Red, endophilin-A1 (PDB ID: 1X03); green, amphiphysin (1URU); blue, arfaptin2 (1I4D). The red and green arcs with indicated diameters represent curved membranes fit the concave surface of endophilin-A1 and amphiphysin, respectively. (**C**) Stereo view of the appendages. Side-chains of the residues forming the hydrophobic ridge and those of interacting with residues of the main body are shown.

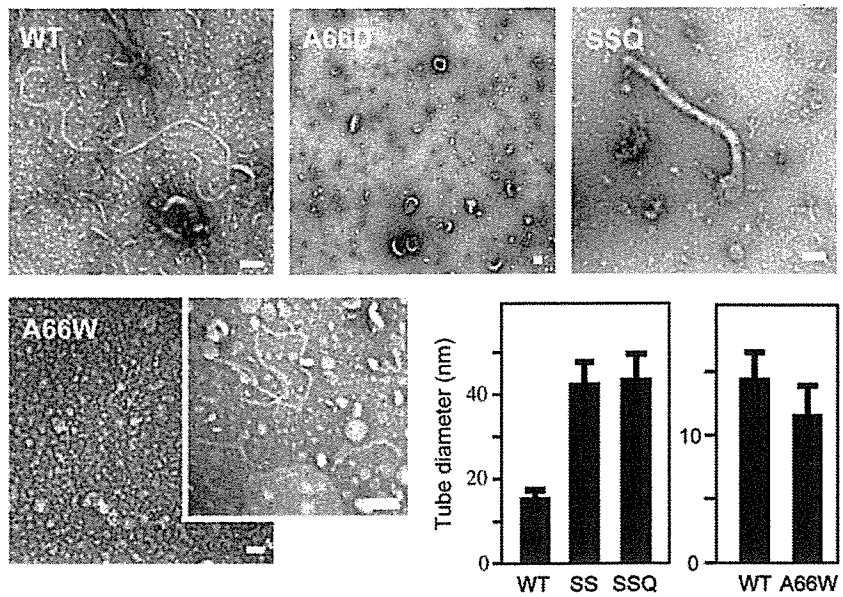

Figure 2 Liposome tubulation by endophilin-A1 BAR domains with mutations in the hydrophobic ridge. WT, 7 μM wild-type BAR domain incubated for 10 min; A66D, 28 μM, 10 min; SSQ, A63S/A66S/M70Q triple mutant, 28 μM, 10 min; A66W, 1.4 μM, 10 min (vesiculated, left panel) and 10 s (tubulated, right panel). Tubulation was not observed when incubated for longer than 1 min. Scale, 100 nm. The bar graphs show tubule diameter (mean and s.d.). SS, A63S/A66S double mutant, 28 μM, 10 min.

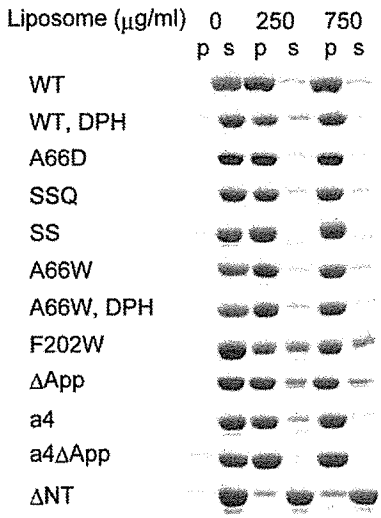

Figure 3 Liposome binding assays of endophilin-A1 BAR domain and its mutants. Protein (200 μg/ml) was co-sedimented with liposomes (0, 250 and 750 μg/ml). Proteins recovered from the pellet (p) and the supernatant (s) were analyzed by SDS–PAGE. The DPH-liposomes show similar binding capacity for the wild type (WT) and the A66W mutants. The liposome binding activity is slightly reduced in the F202W and the appendage-less mutants (ΔApp) and is almost lost in the helix 0 truncated mutant (ΔNT).

(A66W) led to extensive vesiculation and less tubulation. All these mutations did not affect the liposome binding. These results suggest an important role for the hydrophobic ridge in the membrane curvature formation but not in the membrane binding.

Although the ridge reduces the intrinsic curvature of the concave surface (red line in Figure 1B), it appears to promote the membrane curvature formation with conserved hydrophobicity. This raises the possibility that the ridge penetrates into the membrane when the concave surface makes tight contact with the membrane. This possibility was investigated using tryptophan fluorescence, which is sensitive to hydrophobicity of the microenvironment around the indole moiety. The A66W mutant showed 10-nm blueshift of the fluorescence peak in a liposome-dose-dependent and saturable manner, while F202W, a control mutant in which Phe202 on the convex surface was mutated to Trp, did not show any shift (Figure 4A and Supplementary Figure 5). The amount of the blueshift was greater than that observed in 50% DMSO or 50% methanol, indicating that the indol moiety was in a highly hydrophobic environment.

To determine whether this blueshift was caused by the insertion of the indol moiety into the hydrophobic core of the lipid bilayer, we made fluorescence resonance energy transfer (FRET) assays using diphenyl-hexatriene (DPH) as the acceptor probe. DPH has been shown to insert specifically in the nonpolar interior of the membrane and not to alter the membrane structure and dynamics (Repáková *et al*, 2005). DPH liposomes did not affect liposome binding and tubulation (Figure 3 and Supplementary Figure 4). A66W but not F202W showed effective FRET from the 340-nm tryptophan fluorescence (donar) to the DPH fluorescence (acceptor) peaked at 430 nm (Figure 4B and C). It was not caused by changes in the fluorescence property of DPH itself possibly accompanied by tubulation/vesiculation of liposomes (Figure 4D and Supplementary Figure 6). These data suggest that the indol ring of 66W penetrates into the hydrophobic core of the membrane and that the remaining residues of the ridge, about 8 Å in height, appear to be embedded in the layer of lipid head-groups of the contacting membrane leaflet. These results confirmed that the ridge is contacting membrane and that the convex is not contacting membrane surface.

To provide further support for the membrane insertion of the ridge in the wild-type EndA1-BAR, we made a mutant

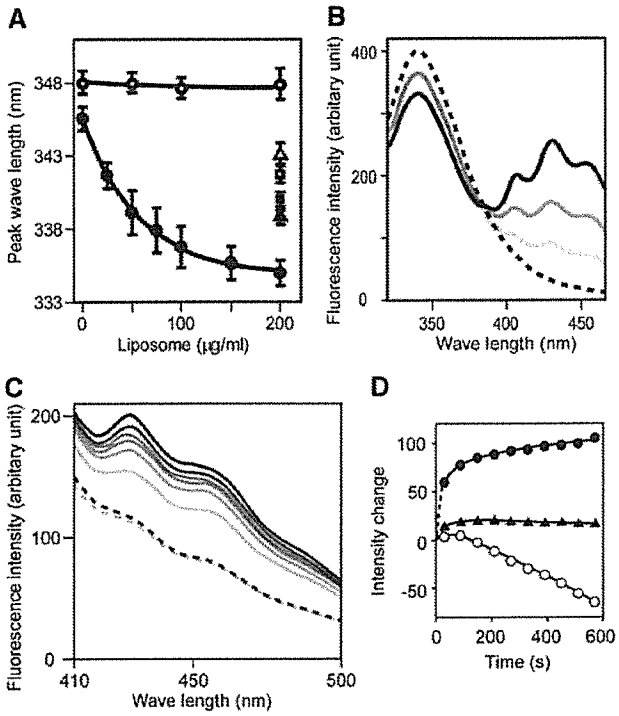

Figure 4 Tryptophan fluorescence blueshift and FRET assays. (**A**) Tryptophan fluorescence emission peak when excited at 280 nm was observed in different concentration of liposome. A66W (●), F202W control mutant (○), A66W alone in 50% DMSO (▲), in 50% MeOH (■), F202W alone in 50% DMSO (△), in 50% MeOH (□), 140 μg/ml protein for all measurements. Mean and s.d. ($N=4$–11). The dose dependency is significant ($P \ll 0.001$) for the A66W mutant but insignificant ($P > 0.8$) for the F202W mutant (one-way ANOVA). DMSO and MeOH were used as blueshift inducer for tryptophan. (**B**) Dose-dependent FRET efficiency from the A66W tryptophan to DPH incorporated in liposomes was examined by the changes of fluorescence. Fluorescence spectrum of A66W (100 μg/ml) with the control liposome (200 μg/ml) excited at 280 nm (hatched). Pale to dark solid curves represent DPH:lipid weight ratios of 1:2000, 1:1000 and 1:500 in the same condition. (**C**) Time-dependent increase in the FRET efficiency from either A66W (pale to dark solid lines, from 30 to 570 s) or F202W tryptophan (pale and dark hatched lines, at 30 and 570 s) to DPH incorporated in liposomes. DPH:lipid weight ratio is 1:500. (**D**) The intensity changes at the 430-nm peak are plotted against time. A66W (●), F202W (▲) excited at 280 nm and A66W (○) excited at 360 nm.

with amphiphysin/arfaptin shape and examined its tubulation activity. The mutant (ΔApp), in which the entire appendage (Q59–Q88) was replaced with a helical stretch (AHLSSLLQ) derived from arfaptin2 sequence (A152–Q159, Y155S), show the crystal structure of a canonical BAR-domain dimer as designed (Figure 5A and Supplementary Figure 7). The ΔApp could bind to liposomes (Figure 3) and cause tubulation to a lesser extent than the wild type and amphiphysin-BAR (Figure 5D and Supplementary Figure 4). As the diameter of the tubules reflects the membrane curvature if the section of the tube is circle, we measured the diameter of the tube to compare the curvature of the EndA1-BAR and its mutant-induced tubes. Despite the higher curvature of the concave surface, the ΔApp dimer induced larger diameter tubules than the wild type did, indicating a positive contribution of the wild-type hydrophobic ridge to drive membrane curvature. Taken all together, the hydrophobic ridge penetrates into the interfacial leaflet of the lipid bilayer when the concave surface is in contact with the membrane and promotes membrane curvature formation.

The BAR domain is rigid enough to impose its intrinsic curvature on membrane

A simple model for the concave surface-driven mechanism is that each BAR domain dimer acts as a molecular mold that impresses its curved surface on the membrane. This model suggests that the membrane curvature approximately mirrors the curvature of the concave surface. Indeed, the diameters of tubules induced by amphiphysin, ΔApp (Figure 5D), SS and SSQ mutants (Figure 2) are compatible with the model-based prediction (see Supplementary Table II for statistical analysis). However, this model has an assumption that the dimer should be rigid enough to overcome the bending resistance of the membrane (Nossal and Zimmerberg, 2002; Farsad and De Camilli, 2003). To examine whether the molecular mold mechanism is feasible, we developed a straight BAR domain by inserting one helical pitch into the helix II in the proximal portion of the extending arm (QSAL is inserted between I154 and Q155). This mutation (a4) would compensate the unequal lengths between helix II and III in the arm, a common feature of the known BAR domain structures, and let the curved arm into a straight one. Although the a4 mutant was designed simply to straighten the curvature of the domain, the structure solved at 2.4 Å resolution shows that it actually has the very interesting property of a flexible arm rather than a rigid one (Figure 5B). Four monomers in the asymmetrical unit show deviation in the bending angles of arms. The blue and the green monomers have straight arms while the orange monomer shows a bending pattern similar to the wild type and the yellow monomer is an intermediate. The structural deviation almost exclusively occurs in the helix kink regions (Supplementary Figure 8), indicating that the arm can swing at least from the bend-free straight position to nearly the wild-type position.

The a4 mutant allowed us to examine how flexibility of the crescent-shaped main body of the BAR dimer affects the membrane curvature formation. The insertion of one helical pitch slightly distorts relative position of the helix II and III (Figure 5C), but does not largely rearrange the spatial positions of the residues on the concave surface of the arm (Supplementary Figure 8). Indeed, the a4 mutant and its appendage-lacking derivative (a4ΔApp) retained normal liposome binding activity (Figure 3). The a4 mutant vesiculated liposomes without any tubulation, while a4ΔApp lost these membrane-deforming activities (Figure 5D and Supplementary Figure 4). The concave surface-induced membrane deforming activity appeared to be lost in the a4 mutant, while the appendage's membrane insertion remained active. These results suggested that the rigidity of the crescent dimer structure is essential for liposome tubulation but not for vesiculation, although appendage insertion induces the vesiclulation.

Roles for the amphipathic helix 0 of the N-BAR domain

The structure of a short amphipathic helix (helix 0) characterizing the N-BAR (Peter *et al*, 2004) can be resolved in the a4 mutant structure due to its tight crystal packing (Figures 5B and 6). The helix 0 is disordered in the wild type (Figure 6) and the ΔApp structures. The helix 0 has been

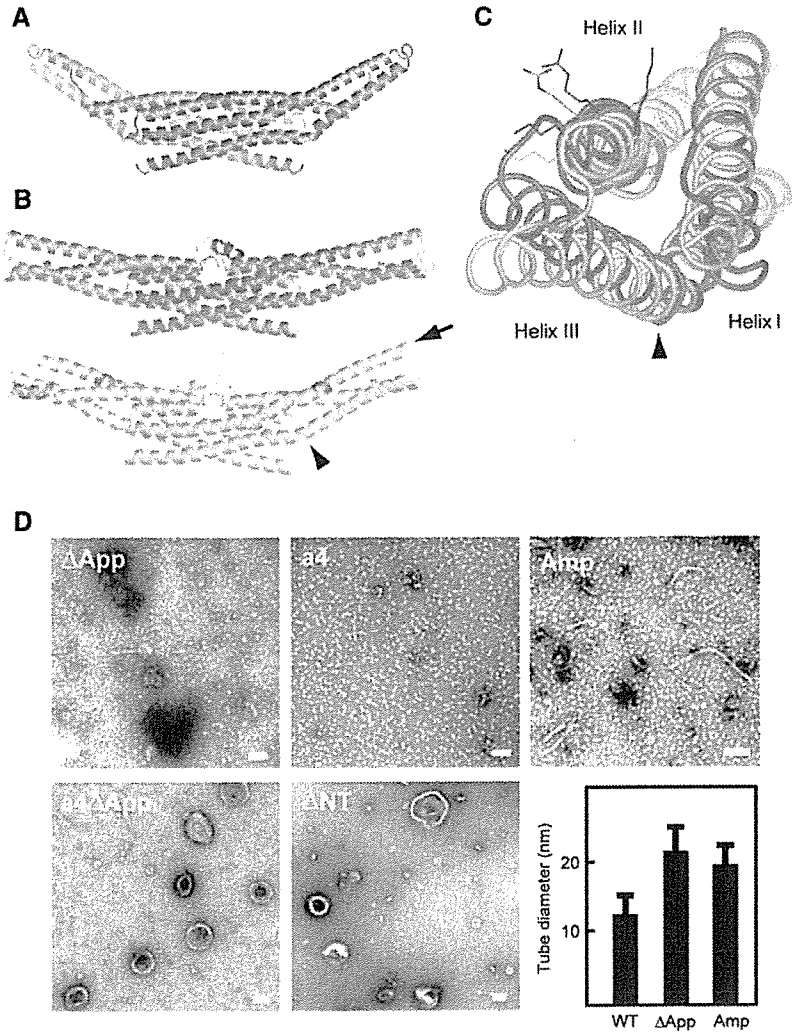

Figure 5 Distinct liposome tubulation induced by endophilin-A1 BAR domain mutants. (**A**) Ribbon representation of a mutated EndA1-BAR dimer lacking the entire appendages (ΔApp, PDB ID: 1X04). The entire appendage (Q59–Q88) was replaced with a helical stretch (AHLSSLLQ) derived from arfaptin2 sequence (A152–Q159, Y155S). Red, mutated segment. (**B**) Ribbon representation of the a4 mutant with swinging arms (PDB ID: 2D4C). One helical pitch was inserted into the helix II in the proximal portion of the extending arm (QSAL was inserted between I154 and Q155). Two dimers in the asymmetrical unit are shown separately. Red, inserted segment; magenta, helix 0. The bending patterns of the helix II and III varies among four monomers. An obvious kink in the helix III remains in the orange monomer (arrowhead, also in (C)). The residual curvature in the blue–green dimer is provided by the intersection of the monomers. (**C**) Superimposition of the a4 mutant monomer (orange one in (B)) and the wild-type monomer (blue) in the core region. A view from the distal end along the helix II (arrow in (B)) shows the maximum structural difference in these arms. Side chains of K171, 173 and R174 are shown. The helix III rotates 12° counterclockwise and shift 6 Å relative to the helix II at the distal end of the arm. The helix 0 and the core region are omitted. (**D**) Negatively stained liposome tubules induced by the BAR domains of endophilin mutants and amphiphysin. ΔApp, 7 μM, incubated for 10 min; a4, 7 μM, 10 min; a4ΔApp, 28 μM, 10 min; ΔNT, 21 μM, 10 min; Amp, 7 μM, 10 min. Note that a4, a4ΔApp, and ΔNT do not induce liposome tubulation. Scale, 100 nm. The bar graph shows tubule diameter (mean and s.d.).

suggested to be helical only when the amphiphysin BAR domain binds to liposomes (Peter *et al*, 2004). The helix 0 displays the hydrophobic branch of T14, V17 and V21 on one side, while K12, K16 and E19 on the other side (Figure 6). The helix 0 is connecting with the Helix I by a flexible linker G23–G24–A25. Consistent with the previous report (Farsad *et al*, 2001), truncation of the helix 0 (ΔNT) resulted in loss of liposome binding activity (Figure 3) and consequently abolished the tubulation (Figure 5D). In contrast, all the helix 0-containing mutants, including the A66D and the a4ΔApp showed intact liposome binding activity irrespective of their tubulation or vesiculation activities. These results indicate that the helix 0 in the endA1-BAR is critical for liposome binding and that the membrane binding of endA1-BAR via helix 0 is not sufficient to induce tubulation or vesiculation.

BAR domain induces tubular membrane deformation in vivo

To explore the significance of the helix 0, the rigid crescent mold, and the appendage of endophilin-A1 BAR domain *in vivo*, we further examined the membrane deformation activity of endophilin-A1 BAR domain in cells (Figure 7). Human umbirical vascular endothelial cells (HUVECs) expressing endophilin-A1 lacking SH3 domain (residues 1–296, hereafter, EndA1-BAR296), which was C-terminally tagged with enhanced green fluorescence protein (EGFP), exhibited intracellular fibrous structure similar to those induced by other BAR domain-containing molecules (Kamioka *et al*, 2004; Itoh *et al*, 2005). Notably, these structures developed from the periphery toward the center of the cells dynamically and disappeared reversibly in living cells (Figure 7E and

Supplementary Movie 1). Furthermore, these GFP-marked structures were co-localized with *in vivo* biotin-labeled membrane (Figure 7D), indicating that EndA1-BAR296-induced fibrous structure seems to be a membrane invagination originated from the plasma membrane. These structures were found in other cells we tested (Figure 7C). In clear contrast, ΔApp, ΔNT and a4 were incapable of inducing membrane deformation in cells, indicating the importance of helix 0, the rigid crescent shape, and the appendage of BAR domain for membrane deformation *in vivo*.

Discussion

The endophilin-A1 BAR domain dimer consists of three sub-modules: the crescent-shaped main body, the helix 0 and the unique appendage. We tried to understand the functional roles for these sub-modules in the membrane curvature formation. In this study by determining the structure of endopholin-A1 BAR domain and developing mutants that were critical for the sub-module structure, we have explored the roles of sub-modules.

Here, we show that the structural rigidity of the crescent-shaped main body is critical for membrane tubulation. The BAR dimer is sufficiently rigid to overcome the bending resistance of the membrane and to be scaffolds for the tubulation (McMahon and Gallop, 2005; Zimmerberg and Kozlov, 2006). The insertion of one helical-pitch into the helix II at distal to the kink brings flexibility to the dimer (a4 mutant). The relative position of the three helices in the

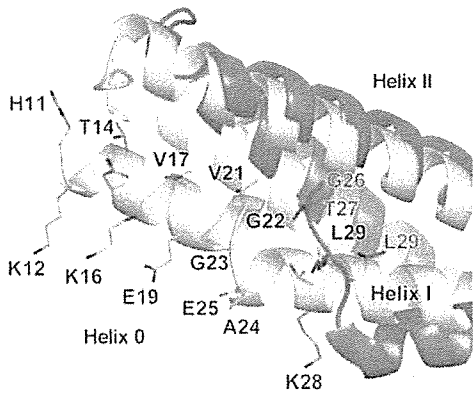

Figure 6 Close-up of helix 0 in an a4 mutant monomer (orange). The same superimposition as in Figure 5C but viewed from the side and displays the helix 0. The helix 0 is disordered in the wild-type structure (blue). The side chains of N-terminal residues are shown (H11KATQKVSEKVGGAEGTKL29 in the a4 and G26TKL in the wild type). The amphipathic helix 0 is stabilized by hydrophobic interactions with the helix II and III and also by hydrogen bonds with a symmetrical molecule.

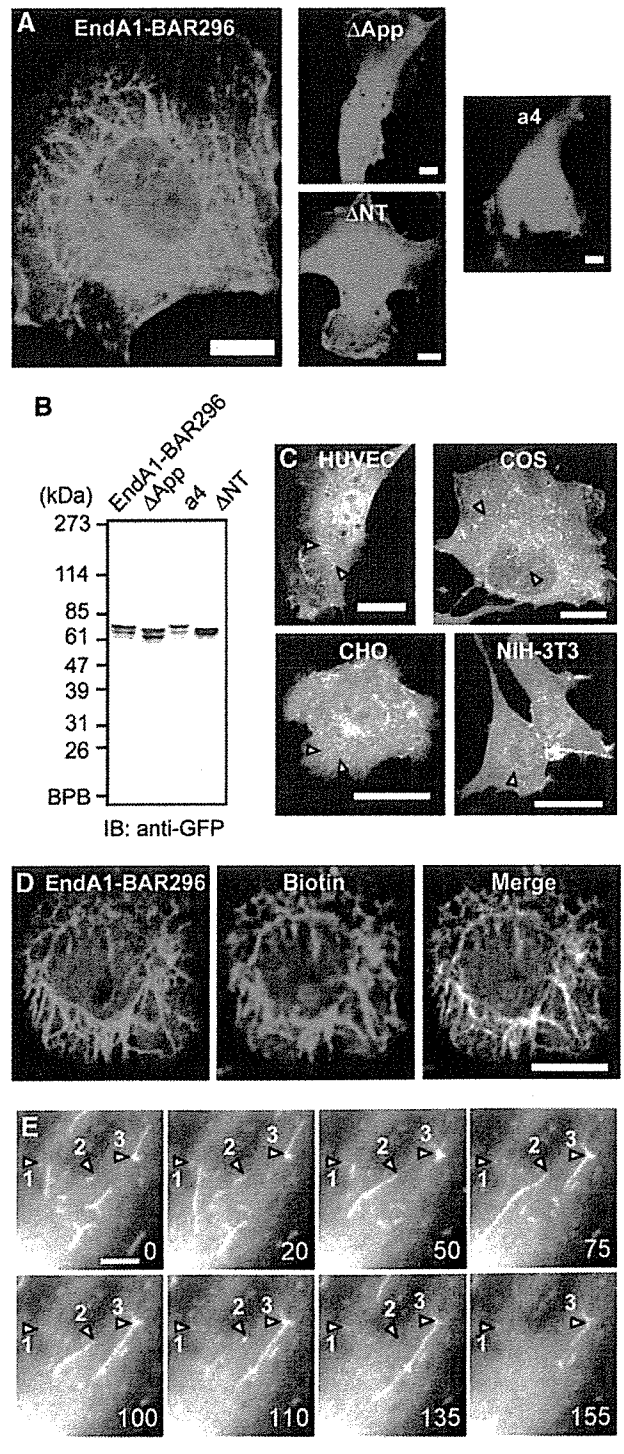

Figure 7 Endophilin A1 BAR domain induces membrane tubulation *in vivo*. (**A**) HUVECs were transfected with plasmids expressing C-teminally EGFP-tagged EndA1-BAR296 (amino acid 1–296 of endophilin-A1), ΔApp, a4, and ΔNT. Cells were GFP-imaged on an epifluorescnce microscope (Olympus IX-71). Fibrous structures were observed exclusively in EndA1-BAR296-expressing cells. Scale, 10 μm. (**B**) Protein expression of the EndA1-BAR296 and the mutants tagged with EGFP in transfected 293T cells were examined by immunoblotted with anti-GFP antibody. (**C**) Cells indicated were similarly transfected to (A). Arrowheads indicate the fibrous structures. Scale, 20 μm. (**D**) Live HUVECs expressing EGFP-tagged EndA1-BAR296 were biotinylated with sulfo-NHS-biotin for 10 min and chased for further 10 min. Covalently bound biotin was visualized using Alexa633-streptavidine. Fluorescnece images for EGFP (left), Alexa633 (center), and merge (right) are shown. Scale, 10 μm. (**E**) A time lapse images of HUVECs expressing EGFP-tagged EndA1-BAR296 were obtained at the time point (seconds) after the observation (Supplementary Movie 1). EGFP-marked structure grows from the cell periphery towards the center of the cell. Notably, both extension and retraction of GFP-marked structure is observed (numbered arrow heads indicate each extending/retracting structure). Scale, 5 μm.

mutant arm was not changed in a4 mutant irrespective of the bend levels (Supplementary Figure 8). The mutant arm behaves as a rigid body and its structure changes only in the vicinity of the helix kinks when it swings. Therefore, it is unlikely that the flexibility of the mutant dimer can be a result of weakened inter-helix interactions in the arm. Moreover, we could not find any specific structural features in the kink region that might explain the flexible hinge in the swinging-arm mutant as well as the rigid bend in the wild-type BAR dimers of endophilin, amphiphysin, and arfaptin.

In this study, for the first time we could determine the structure of the N-terminal amphipathic helix (helix 0) using a swinging-arm mutant. Our mutant and previous mutation analyses indicated that the N-terminal helical sequence of endophilin-A1 is indispensable for liposome binding (Farsad *et al*, 2001), whereas that of amphiphysin is important but not essential for liposome binding and tubulation (Peter *et al*, 2004). The BAR domain of endophilin-A1 is an acidic polypeptide and the cluster of positive charge at the distal end of the arm is not prominent (Figure 1A). This property can explain the critical role for the helix 0 of the EndA1-BAR in liposome binding by providing additional basic residues. The helix 0 structure suggests that K12, K16 and possibly K8 are in a suitable position for cooperation with the positive charge cluster at the distal end. The amphipathic nature of the helix 0 implies that it can also insert into the membrane and facilitate the membrane curvature formation (Peter *et al*, 2004; Gallop and McMahon, 2005; McMahon and Gallop, 2005). Loss of the membrane-deforming activities of the A66D mutant (Figure 2) and the a4ΔApp mutant (Figure 5D) accounts for the additional mechanism for membrane deformation in addition to the membrane insertion of the helix 0.

The N-BAR of endophilins has one additional step to tubulate membrane. Here, we show that the hydrophobic ridge of the endophilin-specific appendage is inserted into the contacting membrane surface. Our data suggested that the entire ridge of the wild-type BAR domain, about 8 Å in height, is embedded in the layer of lipid head-groups of the contacting membrane leaflet. The embedding of the ridge into the membrane is consistent with the local spontaneous curvature mechanism that is reported very recently (Zimmerberg and Kozlov, 2006). As a protruding structure found in epsin1 induces liposome tubulation by being inserted to one leaflet of the lipid bilayer (Ford *et al*, 2002), the penetration of the hydrophobic ridge can drive the positive curvature by causing asymmetrical expansion of the surface area between two leaflets as shown in Figure 8 (Farsad and De Camilli, 2003).

We further explored the importance of the ridge, rigid crescent shape, and helix 0 in cells. We for the first time showed that N-BAR domain induced membrane invaginations originated from plasma membrane, although other BAR-containing molecules have been reported to induce similar invaginations (Itoh *et al*, 2005). Neither mutant that lacked either the ridge or the helix 0 nor flexible mutant formed the tubular invaginations in cells, indicating the significance of these sub-module structure in cells as suggest by *in vitro* studies. We constructed a series of endorphin-A1-EGFP expression plasmids to delineate the domain for the membrane invagination. Full-length endophilin-expressing cells did not show any tubular formation. Because endophilin consists of BAR domain and an SH domain, SH3-binding molecule such as dynamin may inhibit the extension of membrane invagination. This possibility has been suggested in the membrane invagination found in FBP17 and amphiphysin (Kamioka *et al*, 2004; Itoh *et al*, 2005).

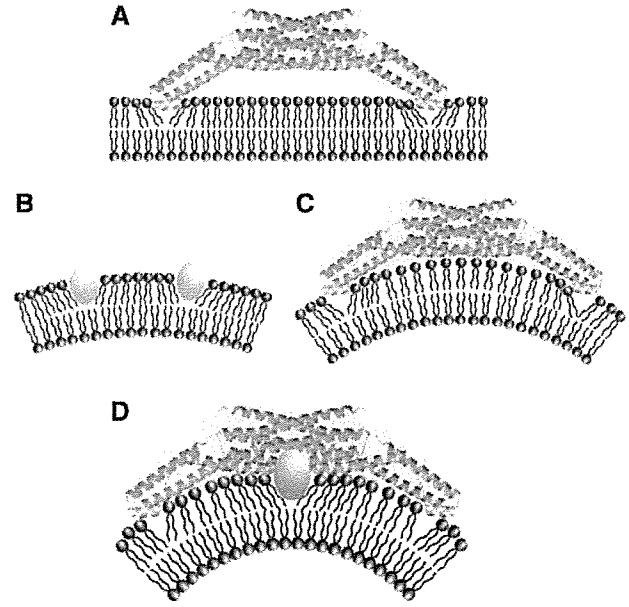

Figure 8 Two potential mechanisms for driving membrane curvature by endophilin-A1. (**A**) Kissing adhesion of an N-BAR domain on planar lipid bilayer. The helix 0 is essential for the membrane binding. Membrane insertion of the helix 0 is supposed. (**B**) Insertion of hydrophobic portions of macromolocules into one leaflet can create bilayer surface discrepancy that causes membrane curvature. (**C**) The simple N-BAR domain, such as amphiphysin and ΔApp, induces membrane curvature by impressing the concave surface onto the membrane. The rigidity of the molecule is required for this mechanism. (**D**) To drive membrane curvature, the endophilin N-BAR domain uses both the rigid crescent shape-mediated deformation and the insertion of hydrophobic ridge on the concave surface in addition to kissing adhesion of N-BAR to membrane surface.

Collectively, EndA1-BAR uses two newly identified mechanisms to drive positive membrane curvature in addition to the essential binding capacity of helix 0 to the membrane: one by the scaffold mechanism common to the BAR domains and the other by the local spontaneous curvature mechanism caused by the membrane insertion of the ridge (Figure 8D). The ridge, which occupies the bottom of the concave lipid-binding surface, may not work until the main body of the BAR dimer localizes itself to a curved membrane. The ridge then inserts into the bilayer roughly perpendicular to the main body, and thus both deformations will occur in the same direction.

Materials and methods

Protein expression and purification by CRECLE

cDNAs encoding BAR domains (amphiphysin1, 1–239; endophilin-A1, 1–247; endophilin-B1, 1–246 in amino-acid residues) were amplified by PCR from a human brain cDNA library. Recombinant proteins were expressed in *Escherichia coli* as GST-fusions using the pGEX6p3 vector, purified by glutathione-Sepharose, cleaved from the GST-tag using Prescission protease (Amersham Biosciences), and further purified by ion-exchange chromatography (Yamagishi *et al*, 2004). The final polypeptide contained an artificial linker

sequence of GPLGS at the N-terminus. EndA1-BAR proteins except for F202W and a4 mutants were purified by crystallization during Prescission protease cleavage. The method, crystallization by regulated cleavage of large hydrophilic tag (CRECLE), was as follows. Purified GST fusions were concentrated to 20–30 mg/ml in an elution buffer (20 mM glutathione, 100 mM Tris–HCl, pH 8.0, 10 mM DTT, 1 mM EDTA, 1 mM EGTA) and then cleaved by a low concentration of prescission protease (1 U/mg protein or less) at 4°C. Slow increase in the tag-free protein concentration might be suitable for crystallization and more than a half of EndA1-BAR protein could be recovered as 20–100 μm microcrystals. They were washed with a low-salt buffer (20 mM HEPES, pH 7.4, 2 mM DTT, 0.2 mM EDTA, 0.2 mM EDTA) and resolved into a high-salt buffer (350 mM NaCl in the low-salt buffer) and used for further analyses.

Protein crystallization

Seleno-methionine (S-Met) derivatives of the EndA1-BAR domain and its appendage-less mutant (ΔApp) were produced in B834(DE3)pLysS cells using Overnight Express Autoinduction System 2 (Novagen). To make X-ray grade crystals in a cryo-ready condition, modified high salt buffer (50 mM HEPES, pH 7.4, 300 mM NaCl, 100 mM KI, 28% ethylene glycol, 5% glycerol, 25 mM DTT) was used. Crystals of 1 mm size were formed by dialysis against 50 mM CHES, pH 9.5, 260 mM NaCl, 28% ethylene glycol, 5% glycerol, 25 mM DTT, 0.4% benzamidine · HCl at 4°C and were flush frozen at 100 K. Crystals could also be grown by vapor diffusion from a similar protein solution using distilled water as the bath solution. The crystals were equilibrated in 50 mM HEPES, pH 7.4, 150 mM NaCl, 25 mM DTT, 0.4% benzamidine · HCl, 5% PEG 8000 and the saturated amount of xylitol as a cryoprotectant. Some of the crystals were soaked with 0.5 mM oleoyl-L-α-lysophosphatidic acid (Sigma) or malonyl-CoA (Sigma) for 4 days with daily change for the substrates. The a4 mutant crystals were grown by sitting-drop vapour diffusion using a bath solution containing 100 mM HEPES, pH 7.2, 200 mM calcium acetate, 10 mM DTT and 20% (w/v) PEG3350 at 20°C and then flush frozen after brief immersion in the same solution containing 16% DMSO. The wild type and the ΔApp mutant crystals belong to the same space group $I4_1$ and contain one monomer molecule in the asymmetric unit (Supplemental Figure 1). The a4 crystal belongs to $P2_1$ and contains two dimers in the asymmetric unit.

Structural determination

The EndA1-BAR structure was determined using the multiple anomalous dispersion (MAD) method. Multiple-wavelength X-ray diffraction data sets were collected from a single Se-Met crystal (crystal I) at SPring-8 beamline BL44B2 (Supplementary Table I). Single wavelength data sets of another crystal (crystal II) and of a ΔApp crystal used for the refinement were collected at BL45PX. The data set for the a4 mutant was collected at BL38B1. All diffraction data sets were collected at 90 K and were processed using HKL2000 suite (Otwinowski and Minor, 1997). The seven positions out of 10 expected selenium atoms were identified by SOLVE (Terwilliger and Berendzen, 1999). The initial phases calculated by SOLVE with a figure of merit of 0.59 at 3.2 Å resolution were further improved by RESOLVE (Terwilliger, 1999). The density modified MAD map (Supplementary Figure 1) had sufficient quality to trace the polypeptide chain except for the N-terminus and the loop region of the appendage. The model was built with TURBO-FRODO (Roussel and Cambillau, 1996) and refined to the resolutions of 3.1 Å by CNS (Brunger *et al*, 1998). The final model includes 210 residues (residues 26–71 and 84–247), and has an *R* factor of 23.6% (R_{free} of 26.4%). The ΔApp structure was solved by molecular replacement by MOLREP in the CCP4 suite (CCP4, 1994) and refined to the resolution of 2.9 Å by CNS. The simulated annealing omit electron density map calculated by CNS confirmed the continuous α-helical structure of the replaced region as designed (Supplementary Figure 7). The final model includes 200 amino-acid residues and has an *R* factor of 23.8% (R_{free} of 26.9%). The a4 mutant structure was solved by molecular replacement using the central core of the EndA1-BAR as a starting model and the arms were manually built (Supplementary Figure 7). The structure was refined to the resolution of 2.4 Å by CNS with an *R* factor of 21.5% (R_{free} of 26.9%). Main-chain dihedral angles of all non-glycine residues of these three models lie in allowed regions of the Ramachandran plot, with 94.3% for the EndA1-BAR, 94.1% for the ΔApp mutant, and 96.4% for the a4 mutant in most-favored regions, respectively. Graphical representations were prepared using the programs TURBO-FRODO, MOLSCRIPT (Kraulis, 1991), RASTER3D (Merritt and Bacon, 1997), GRASP (Nicholls *et al*, 1991) and Pymol (DeLano, 2002).

Liposome binding and tubulation assays

Liposome sedimentation assay and tubulation assay were as earlier described (Peter *et al*, 2004 see also McMahon lab protocols: http://www2.mrc-lmb.cam.ac.uk/NB/McMahon_H/group/techniqs/techniqs.htm) with slight modifications. Briefly, Folch fraction 1 (Sigma) was used as the lipid source and liposome suspension, 1 mg/ml in liposome buffer (20 mM HEPES, pH 7.4, 150 mM NaCl, 1 mM DTT) was made by sonication. Freshly purified BAR domain proteins were diluted at about 1 mg/ml in the liposome buffer and ultracentrifuged at 400 000 *g* for 10 min just before use. No crystallization occurred at this or lower concentrations. For sedimentation assays, 20 μg proteins were mixed with 25 or 75 μg liposomes in 100 μl of the liposome buffer, incubated for 10 min on ice and ultracentrifuged at 200 000 *g* for 10 min. For tubulation assays, 400 μg/ml proteins were mixed with an equal volume of 400 μg/ml liposomes, left for 10 s to 30 min at room temperature, and then processed for negative staining. Judging from the liposome sedimentation and the tryptophan fluorescence assays, this protein to lipid ratio ensured nearly saturated protein–liposome binding. Magnification was calibrated using a grating replica of 2160/mm.

Tryptophan fluorescence and FRET assay

Fluorescence emission spectra were recorded with a Hitachi F-4500 fluorescence spectrophotometer (Ohki *et al*, 2004). For tryptophan fluorescence assays, 140 μg/ml tryptophan-containing mutants were mixed with 0–200 μg/ml liposomes in the liposome buffer, incubated for 3 min, and excited at 280 nm. For FRET assays, DPH-liposomes were made by adding DPH (Molecular Probe) into lipid solution (1:500 to lipid, w:w). The fluorescence of DPH-liposomes (200 μg/ml) excited at 280 nm was scanned from 400 to 500 nm at 1-min intervals. The first measurement of the 430-nm DPH peak was obtained at about 30 s after mixing with mutant proteins (100 μg/ml).

Cell culture, transfection and surface biotinylation

HUVECs were purchased from Kurabo and cultured in HuMedia-EG2 as described previously (Sakurai *et al*., 2006). 293T cells, CHO cells, Cos7 cells, and NIH-3T3 cells were cultured in DMEM supplemented with 10% fetal bovine serum as described previously (Kamioka *et al*., 2004). Cells were transfected using LipofectAMINE 2000 (Invitrogen). Live HUVECs were biotinylated with 5 mM sulfo-NHS-biotin (Pierce) in Opti-MEM (Invitrogen) for 10 min. They were washed once with Opti-MEM and chased for 10 min with the normal culture medium, and fixed with 2% formaldehyde after a brief wash with Opti-MEM containing 1/20 volume of Avidin D blocking solution (Vector Laboratory) to reduce the cell surface background staining. HUVECs were permeabilized with cold MeOH and biotin was visualized using Alexa633-streptavidine (Molecular Probe).

Supplementary data

Supplementary data are available at *The EMBO Journal* Online.

Acknowledgements

We thank H Nakajima, T Matsu, Y Kawano and H Naitow for technical assistance with SPring-8 beamlines, and H Ago and M Miyano, Structural Biophysics Laboratory, RIKEN Harima Institute at SPring-8, for their helpful advice. This work was supported in part by Grant for Research on Advanced Medical Technology from the Ministry of Health, Labour, and Welfare of Japan, by the Program for Promotion of Fundamental Studies in Health Sciences of the National Institute of Biomedical Innovation (NIBIO), and by Special Coordination Funds for Promoting Science and Technology, Ministry of Education, Culture, Sports, Science and Technology (MEXT) of Japan.

Competing interests statement

The authors declare that they have no competing commercial interests in relation to this work.

References

Brunger AT, Adams PD, Clore GM, DeLano WL, Gros P, Grosse-Kunstleve RW, Jiang JS, Kuszewski J, Nilges M, Pannu NS, Read RJ, Rice LM, Simonson T, Warren GL (1998) Crystallography & NMR system: a new software suite for macromolecular structure determination. *Acta Crystallogr D* **54:** 905–921

Collaborative Computational Project Number 4 (1994) The CCP4 suite: programs for protein crystallography. *Acta Crystallogr D* **50:** 760–763

DeLano WL (2002) *The PyMOL User's Manual.* DeLano Scientific: San Carlos, CA, USA

Galli T, Haucke V (2004) Cycling of synaptic vesicles: How far? How fast!. *Sci STKE* **2004:** re19

Farsad K, Ringstad N, Takei K, Floyd SR, Rose K, De Camilli P (2001) Generation of high curvature membranes mediated by direct endophilin bilayer interactions. *J Cell Biol* **155:** 193–200

Farsad K, De Camilli P (2003) Mechanisms of membrane deformation. *Curr Opin Cell Biol* **15:** 372–381

Ford MG, Mills IG, Peter BJ, Vallis Y, Praefcke GJ, Evans PR, McMahon HT (2002) Curvature of clathrin-coated pits driven by epsin. *Nature* **419:** 361–366

Gallop JL, McMahon HT (2005) BAR domains and membrane curvature: bringing your curves to the BAR. *Biochem Soc Symp* **72:** 223–231

Habermann B. (2004) The BAR-domain family of proteins: a case of bending and binding. *EMBO Rep* **5:** 250–255

de Heuvel E, Bell AW, Ramjaun AR, Wong K, Sossin WS, McPherson PS (1997) Identification of the major synaptojanin-binding proteins in brain. *J Biol Chem* **272:** 8710–8716

Itoh T, Erdmann KS, Roux A, Habermann B, Werner H, De Camilli P (2005) Dynamin and the actin cytoskeleton cooperatively regulate plasma membrane invagination by BAR and F-BAR proteins. *Dev Cell* **9:** 791–804

Kamioka Y, Fukuhara S, Sawa H, Nagashima K, Masuda M, Matsuda M, Mochizuki N. (2004) A novel dynamin-associating molecule, formin-binding protein 17, induces tubular membrane invaginations and participates in endocytosis. *J Biol Chem* **279:** 40091–40099

Karbowski M, Jeong SY, Youle RJ (2004) Endophilin B1 is required for the maintenance of mitochondrial morphology. *J Cell Biol* **166:** 1027–1039

Kraulis PJ (1991) MOLSCRIPT: a program to produce both detailed and schematic plots of protein structure. *J Appl Crystallogr* **24:** 946–950

McMahon HT, Mills IG (2004) COP and clathrin-coated vesicle budding: different pathways, common approaches. *Curr Opin Cell Biol* **16:** 379–391

McMahon HT, Gallop JL (2005) Membrane curvature and mechanisms of dynamic cell membrane remodeling. *Nature* **438:** 590–596

Merritt EA, Bacon DJ (1997) Raster3D: photorealistic molecular graphics. *Methods Enzymol* **277:** 505–524

Modregger J, Schmidt AA, Ritter B, Huttner WB, Plomann M (2003) Characterization of Endophilin B1b, a brain-specific membrane-associated lysophosphatidic acid acyl transferase with properties distinct from endophilin A1. *J Biol Chem* **278:** 4160–4167

Nicholls A, Sharp K, Honig B (1991) Protein folding and association: insights from the interfacial and thermodynamic properties of hydrocarbons. *Proteins* **11:** 281–296

Nossal R, Zimmerberg J (2002) Endocytosis: curvature to the ENTH degree. *Curr Biol* **12:** R770–R772

Ohki T, Mikhailenko SV, Morales MF, Onishi H, Mochizuki N (2004) Transmission of force and displacement within the myosin molecule. *Biochemistry* **43:** 13707–13714

Otwinowski Z, Minor W (1997) Processing of X-ray diffraction data collected in oscillation mode. *Methods Enzymol* **276:** 307–326

Peter BJ, Kent HM, Mills IG, Vallis Y, Butler PJ, Evans PR, McMahon HT (2004) BAR domains as sensors of membrane curvature: the amphiphysin BAR structure. *Science* **303:** 495–499

Repáková J, Holopainen JM, Morrow MR, McDonald MC, Capkova P, Vattulainen I (2005) Influence of DPH on the structure and dynamics of a DPPC bilayer. *Biophys J* **88:** 3398–3410

Ringstad N, Nemoto Y, De Camilli P (1997) The SH3p4/Sh3p8/SH3p13 protein family: binding partners for synaptojanin and dynamin via a Grb2-like Src homology 3 domain. *Proc Natl Acad Sci USA* **94:** 8569–8574

Ringstad N, Nemoto Y, De Camilli P (2001) Differential expression of endophilin 1 and 2 dimers at central nervous system synapses. *J Biol Chem* **276:** 40424–40430

Roussel A, Cambillau C (1996) *TURBO-FRODO Manual.* Marseille France AFMB-CNRS, Paris, France

Sakurai A, Fukuhara S, Yamagishi A, Sako K, Kamioka Y, Masuda M, Nakaoka Y, Mochizuki N (2006) MAGI-1 is required for Rap1 activation upon cell–cell contact and for enhancement of vascular endothelial cadherin-mediated cell adhesion. *Mol Biol Cell* **17:** 966–976

Schuske KR, Richmond JE, Matthies DS, Davis WS, Runz S, Rube DA, van der Bliek AM, Jorgensen EM (2003) Endophilin is required for synaptic vesicle endocytosis by localizing synaptojanin. *Neuron* **40:** 749–762

Tarricone C, Xiao B, Justin N, Walker PA, Rittinger K, Gamblin SJ, Smerdon SJ (2001) The structural basis of Arfaptin-mediated cross-talk between Rac and Arf signalling pathways. *Nature* **411:** 215–219

Terwilliger TC (1999) Reciprocal-space solvent flattening. *Acta Crystallogr D* **55:** 1863–1871

Terwilliger TC, Berendzen J (1999) Automated MAD and MIR structure solution. *Acta Crystallogr D* **55:** 849–861

Verstreken P, Koh TW, Schulze KL, Zhai RG, Hiesinger PR, Zhou Y, Mehta SQ, Cao Y, Roos J, Bellen HJ (2003) Synaptojanin is recruited by endophilin to promote synaptic vesicle uncoating. *Neuron* **40:** 733–748

Weissenhorn W (2005) Crystal structure of the endophilin-A1 BAR domain. *J Mol Biol* **351:** 653–661

Wenk MR, De Camilli P (2004) Protein–lipid interactions and phosphoinositide metabolism in membrane traffic: insights from vesicle recycling in nerve terminals. *Proc Natl Acad Sci USA* **101:** 8262–8269

Yamagishi A, Masuda M, Ohki T, Onishi H, Mochizuki N (2004) A novel actin-bundling/filopodium-forming domain conserved in insulin receptor tyrosine kinase substrate p53 and missing in metastasis protein. *J Biol Chem* **279:** 14929–14936

Zimmerberg J, Kozlov MM (2006) How proteins produce cellular membrane curvature. *Nat Rev Mol Cell Biol* **7:** 9–19